Native frames: An approach for separating sequential and concerted three-body fragmentation

T. Severt, Jyoti Rajput, Ben Berry, Bethany Jochim, Peyman Feizollah, Balram Kaderiya, M. Zohrabi, Farzaneh Ziaee, Kanaka Raju P., D. Rolles, A. Rudenko, K. D. Carnes, B. D. Esry, and I. Ben-Itzhak

Phys. Rev. A **110**, 053104 — Published 12 November 2024

DOI: 10.1103/PhysRevA.110.053104

Native frames: An approach for separating sequential and concerted three-body fragmentation

T. Severt, Jyoti Rajput,* Ben Berry, Bethany Jochim, Peyman Feizollah, Balram Kaderiya, M. Zohrabi, Farzaneh Ziaee, Kanaka Raju P.,† D. Rolles, A. Rudenko, K. D. Carnes, B. D. Esry, and I. Ben-Itzhak‡
J. R. Macdonald Laboratory, Physics Department,
Kansas State University, Manhattan, Kansas 66506
(Dated: October 15, 2024)

Disentangling sequential and concerted three-body fragmentation has been a long-standing endeavor in studies of molecular dynamics. To accomplish this goal, we recently introduced a novel method to separate sequential from concerted breakup, where the sequential events are analyzed in their native frames [J. Rajput *et al.*, Phys. Rev. Lett. **120**, 103001 (2018)]. The essence of this method is the use of the Jacobi coordinates' conjugate momenta to reduce the dimensionality of the multi-body fragmentation in combination with a clear signature for sequential breakup. To demonstrate this method, we employ coincidence momentum imaging to study the strong-field dissociative ionization of OCS into $O^+ + C^+ + S^+$, which typically undergoes concerted fragmentation or sequential breakup involving either a metastable CO^{2+} or CS^{2+} molecule. We identify sequential breakup using a uniform distribution as a function of the angle between the conjugate momenta, associated with the first and second fragmentation steps, which is due to the rotation of the intermediate molecule in the fragmentation plane. By exploiting this uniform distribution, we separate the sequential and concerted distributions in any plot created from the measured momenta.

I. INTRODUCTION

When a molecule or cluster is ionized, the propagation of the dissociating wavepacket on the potential energy landscape determines the dynamics leading to fragmentation. Many experimental techniques image the asymptotic momentum distributions of the resulting fragments to learn about the evolution of the system following ionization. Due to the complexity of even the simplest of molecules, extracting information about the fragmentation dynamics is challenging and is a longstanding goal of the molecular dynamics community, e.g., see [1–24].

On occasion, researchers try to identify specific dynamical processes using signatures found in the final momentum distributions. One such example is the sequential fragmentation of polyatomic molecules, where two or more chemical bonds break in a stepwise fashion. Between the fragmentation steps, the intermediate metastable molecule may rotate, providing a signature to distinguish sequential from concerted breakup, in which all bonds break quickly relative to the rotational period of the molecule [25, 26].

For example, separating concerted from sequential breakup distributions is vital for interpreting many experiments, especially when invoking the axial-recoil approximation [27]. One relevant example is the transformation of the recoil-frame photoelectron angular distributions (RFPADs) to the molecular-frame photoelectron angular distributions (MFPADs) [14, 17, 28–30] for data containing sequential fragmentation [31]. If the intermediate molecule (hereafter referred to as "intermediate" in short) rotates for some time after ionization, the intermediate's asymptotic heavy-particle momenta no longer determine the orientation of the molecule at the time of ionization. However, the momentum of the first ejected heavy fragment may relate to that initial orientation. Therefore, choosing the fragment not involved in the rotation as a reference to define the RFPAD [31] allows for a more meaningful interpretation of the RFPAD distribution. Furthermore, to obtain meaningful MFPAD distributions, it is vital to first eliminate any sequential fragmentation contributions.

Since sequential breakup results in the breakdown of the axial-recoil approximation, it poses additional difficulties when interpreting photofragmentation angular distributions relative to the polarization of the light [32, 33], or relative angular distributions between fragments [34–36]. These examples show the need for a technique that allows not only the identification of sequential fragmentation but also its separation and subtraction from other competing processes, leading to separate sequential- and concerted-breakup plots. It is worth noting, however, that events contained in the remaining concerted fragmentation distribution do not necessarily satisfy the axial recoil approximation [37, 38]. In some instances, researchers have shown that the final momentum distributions of concerted breakup can be dramatically different than what is naively expected based on the initial geometry of the molecule [39, 40]. Finally, given that in this study intense laser pulses are used to initiate the fragmentation, we note that the laser pulse itself may cause the breakdown of the axial recoil approximation, even in two-body breakup [41].

For the past few decades, researchers have used a variety of strategies to distinguish sequential from concerted

* Permanent address: Department of Physics and Astrophysics, University of Delhi, Delhi 110007, India.
† Present address: School of Quantum Technology, DIAT(DU), Pune, India 411025
‡ ibi@phys.ksu.edu

three-body fragmentation in molecular breakup [18, 25, 26, 31, 34, 37, 42–65]. Furthermore, identifying three-body sequential breakup finds applications in other fields, including the study of the decay of mesons [66–68] and nuclear fragmentation [69–74]. A specific nuclear fragmentation example is the decay of the Hoyle state [69–73], where ^{12}C predominantly decays sequentially into three α particles via an intermediate ^{8}Be*.

To distinguish sequential from concerted breakup, the coincident three-dimensional momentum imaging of the resulting breakup is typically crucial. Of the many plotting strategies developed to recognize sequential fragmentation [18, 31, 34, 44–65], Dalitz plots and Newton diagrams became the gold standards for identifying and even partially separating sequential from concerted breakup [18, 31, 44, 50–65].

Improving on Dalitz plots and Newton diagrams, we recently demonstrated a novel analysis method enabling the separation of sequential and concerted breakup by studying three-body sequential fragmentation in the "native frame" of each step [37]. By plotting the distribution of angles between the conjugate momenta of the Jacobi coordinates [75–79], sequential fragmentation is identified as a uniform angular distribution due to the rotation of the intermediate molecule in the fragmentation plane, which is defined by the measured momenta of the fragments. Furthermore, we can reconstruct the parts of the sequential fragmentation distribution masked by concerted and other sequential-breakup processes by exploiting this uniform angular distribution. Finally, we separate the concerted fragmentation distributions by subtracting all possible sequential breakup contributions from the complete data set [37].

In this paper, we describe the native-frames method introduced in Ref. [37] in greater detail and highlight the wide variety of information revealed by such analysis, using the dissociative triple ionization of OCS (i.e., the linear carbonyl sulfide, O=C=S [80]) as an example. In particular, we study the fragmentation of OCS into $O^+ + C^+ + S^+$, which undergoes two possible sequential pathways involving either a CO^{2+} or CS^{2+} intermediate metastable molecule [55, 61, 62]. The native-frames method is not unique to OCS and applies to many systems, not only molecules that undergo sequential three-body fragmentation. Neither is it limited to charged fragments, as illustrated by its recent application to the three-body breakup of water dications, where the neutral fragment momentum was derived from momentum conservation [81, 82]. The generality of the native frames analysis approach stems from the use of the Jacobi coordinates' conjugate momenta to reduce the dimensionality of the data and analyze it systematically, as well as provide a framework to generalize toward fragmentation processes involving more than three fragments.

II. EXPERIMENTAL METHOD

In our experiment, an ultrafast intense laser field initiates triple ionization and dissociation of OCS molecules. Briefly, we produce the laser pulse using an ultrafast Ti:Sapphire chirped-pulse-amplification laser system (KMLabs) with a 10-kHz repetition rate, maximum pulse energy of 2 mJ, central wavelength of 790 nm, and a pulse duration of 23 fs (full-width-half-maximum in intensity).

About 180 μJ of the laser beam is focused onto a supersonic jet using a spherical mirror ($f = 7.5$ cm), producing a peak intensity of $(5.6 \pm 0.8) \times 10^{14}$ W/cm^2. The peak intensity is determined by measuring the recoil momentum distributions of Ne^+ ions along the laser polarization in an independent experiment. Then, we identify the "kink" in the kinetic energy distribution associated with twice the pondermotive energy, which indicates the transition where rescattered electrons become dominant over the direct electrons [83].

We employ the cold-target-recoil-ion-momentum-spectroscopy (COLTRIMS) technique [6, 8] to measure all charged atomic and molecular products of OCS in coincidence, using a time- and position-sensitive detector, allowing us to compute the three-dimensional momentum distributions. To limit the total count rate on the detector and further cool the OCS molecules in the supersonic jet, we add a He buffer gas at a partial-pressure ratio of 99 to 1 (He to OCS, with an estimated density of the order of 10^8–10^9 particles/cm^3).

The main channel of interest in this work is the three-body breakup of OCS into $O^+ + C^+ + S^+$. In addition, we analyze the two-body $CO^{2+} + S^+$ and $CS^{2+} + O^+$ fragmentation channels. These channels are effectively a subset of sequential fragmentation events where the metastable intermediate dications, CO^{2+} or CS^{2+}, do not dissociate before striking the detector — i.e., the metastable state's lifetime is longer than its few microsecond time-of-flight (TOF) to the detector. It is important to note that we analyze all fragmentation channels included in this paper in the center-of-mass (CM) frame of reference of the recoiling OCS^{3+} molecule.

III. IDENTIFYING SEQUENTIAL FRAGMENTATION

To determine if three-body sequential fragmentation occurs, previous studies identified its signatures in Newton diagrams and Dalitz plots [18, 31, 44, 50–65]. In Fig. 1, we show an example Newton diagram and Dalitz plot for the three-body fragmentation of OCS into $O^+ + C^+ + S^+$ with marked features associated with sequential breakup involving the intermediate CO^{2+} and CS^{2+} molecules.

In the case of the Newton diagram, which is a momentum correlation map of the three fragments, the signature of sequential fragmentation is a circular feature, which is attributed to the rotation of the intermediate molecule

in the fragmentation plane [50]. For OCS fragmentation, when plotting the Newton diagram with the S^+ momentum fixed to the x axis, as shown in Fig. 1(a), sequential breakup involving the CO^{2+} intermediate emerges as offset semicircles. On the other hand, sequential fragmentation involving the CS^{2+} intermediate is a "sprinkler"-like feature, as indicated by the dotted line determined from the distribution of this sequential channel after separation from competing channels, as described in Sec. VI B. To make sequential breakup involving the CS^{2+} intermediate appear as semi-circular features, one must create a Newton plot with the O^+ momentum fixed to the x axis instead.

The Dalitz plot [66], which displays the energy sharing among the fragments, is another plotting method used to identify sequential fragmentation. The typical signature of sequential breakup, including in our case, is a distribution following a straight line that spans the range allowed by momentum conservation, as shown for three-body OCS fragmentation in Fig. 1(b). The distributions appear as straight lines due to the rotation of the intermediate molecule in the fragmentation plane and energy conservation, which forces the kinetic energies of each fragment of the intermediate molecule, in the CM of the parent molecular ion, to depend on the final breakup angle relative to the first step. In other words, the kinetic energy of a fragment is larger or smaller if it breaks in the same or opposite direction of the intermediate molecule's CM momentum, respectively. Additionally, the energy of each fragment changes as a function of the breakup angle, filling in the distribution along the line. The Dalitz plot has been used to separate a subset of the sequential breakup from the concerted fragmentation events to learn more about the steps of the sequential breakup [57, 59] and address the enhancement or suppression of sequential fragmentation rates under different experimental conditions [61].

Since three-body sequential fragmentation occurs in two steps, it is natural to study it in the native frames of reference associated with the first and second breakup steps [37]. In this section, we derive the conjugate momenta of the Jacobi coordinates, which are the natural coordinates describing the native frames of reference and have long been used to study few-body systems [75–79]. Furthermore, we show that identifying sequential fragmentation processes using the native-frames method reduces to choosing one of the several possible Jacobi sets, specifically demonstrated on OCS as an example.

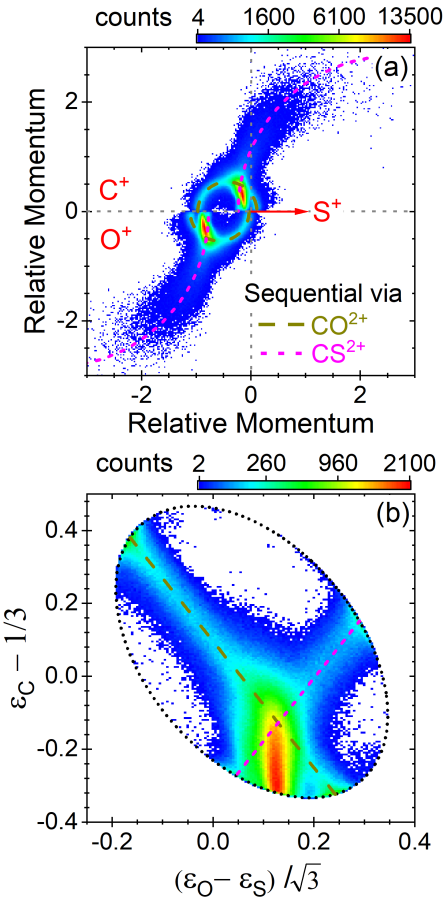

FIG. 1. (Color online) (a) Newton diagram for the three-body fragmentation of OCS into $O^+ + C^+ + S^+$. The momentum of the S^+ fragment is chosen to be along the x axis. The C^+ and O^+ momenta are divided by $|\boldsymbol{P}_S|$ and placed in the upper and lower halves of the plot, respectively. The black dashed offset semicircles represent the sequential fragmentation process via the CO^{2+} intermediate. The magenta dashed lines represent the sequential fragmentation process via the CS^{2+} intermediate determined from our analysis presented in Sec. VI B. (b) The Dalitz plot with straight black and magenta dashed lines representing the expected energy relation for sequential fragmentation via the CO^{2+} and CS^{2+} intermediate molecules, respectively. Specifically, ε_i represents the scaled energy of fragment i, that is the kinetic energy of that fragment divided by the total kinetic energy released by all the measured atomic fragments. The black dotted oval represents the boundaries determined by momentum conservation. These density plots, and all others density plots in this paper, show the number of events, N, on a $\sqrt{N}$ scale and their color bar indicates the counts scale.

A. Defining the native frames of reference

The native frames allows one to reduce the dimensionality of the multi-body fragmentation process observed by using the Jacobi coordinates [75–79] and their conjugate momenta to analyze momentum imaging data. The benefits of the simplification of the data, by reducing the number of dimensions, is widely applicable and can be naturally extended to a larger number of fragments. We guide one through the application of this method in detail using three-body fragmentation of OCS^{3+} as an example.

Consider the sequential three-body fragmentation of an arbitrary ABC molecule, where the two breakup steps

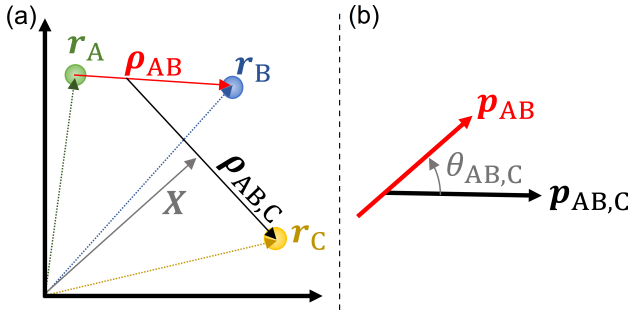

FIG. 2. (Color online) (a) Definition of the Jacobi coordinates, $\boldsymbol{\rho}_{\mathrm{AB,C}}$ and $\boldsymbol{\rho}_{\mathrm{AB}}$, as well as the CM position vector $\boldsymbol{X}$, for an arbitrary ABC molecule in some laboratory-fixed frame [75–79]. (b) The definition of the angle $\theta_{\mathrm{AB,C}}$ between the relative momenta, $\boldsymbol{p}_{\mathrm{AB}}$ and $\boldsymbol{p}_{\mathrm{AB,C}}$ (see text).

are given by

$$\begin{aligned} \mathrm{ABC} &\rightarrow \mathrm{AB} + \mathrm{C} \qquad (1^{\mathrm{st}}\ \mathrm{step}), \\ \mathrm{AB} &\rightarrow \mathrm{A} + \mathrm{B} \qquad (2^{\mathrm{nd}}\ \mathrm{step}), \end{aligned}$$

and the three-dimensional momenta of all fragments are measured in coincidence [84]. In the first step, the energy deposited into the system leads to the breakup of the ABC molecule into AB + C, where the AB molecule is in a distribution of rovibrational (and possibly electronic) states, some of which are metastable with a corresponding lifetime. In the second step, these metastable states dissociate into A + B after rotating for some time that typically exceeds their lifetime.

To analyze sequential breakup, we begin with the Jacobi coordinates [75–79], shown schematically in Fig. 2(a). These coordinates are

$$\boldsymbol{\rho}_{\mathrm{AB,C}} = \boldsymbol{r}_{\mathrm{C}} - \frac{1}{m_{\mathrm{AB}}}\left(m_{\mathrm{A}}\boldsymbol{r}_{\mathrm{A}} + m_{\mathrm{B}}\boldsymbol{r}_{\mathrm{B}}\right), \tag{1}$$

$$\boldsymbol{\rho}_{\mathrm{AB}} = \boldsymbol{r}_{\mathrm{B}} - \boldsymbol{r}_{\mathrm{A}}, \tag{2}$$

where $\boldsymbol{\rho}_{\mathrm{AB,C}}$ and $\boldsymbol{\rho}_{\mathrm{AB}}$ represent the relative position vectors. Note that the comma, in this notation, separates the molecular fragments moving apart. The position of the CM of the ABC molecule is

$$\boldsymbol{X} = \frac{1}{M}\left(m_{\mathrm{A}}\boldsymbol{r}_{\mathrm{A}} + m_{\mathrm{B}}\boldsymbol{r}_{\mathrm{B}} + m_{\mathrm{C}}\boldsymbol{r}_{\mathrm{C}}\right). \tag{3}$$

The total mass of the intermediate AB molecule is

$$m_{\mathrm{AB}} = m_{\mathrm{A}} + m_{\mathrm{B}}, \tag{4}$$

and the total mass of the parent ABC molecule is

$$M = m_{\mathrm{AB}} + m_{\mathrm{C}}. \tag{5}$$

From Eq. (1), the conjugate momentum of $\boldsymbol{\rho}_{\mathrm{AB,C}}$ is

$$\boldsymbol{p}_{\mathrm{AB,C}} = \mu_{\mathrm{AB,C}}\,\dot{\boldsymbol{\rho}}_{\mathrm{AB,C}} = \frac{m_{\mathrm{AB}}}{M}\boldsymbol{P}_{\mathrm{C}} - \frac{m_{\mathrm{C}}}{M}\left(\boldsymbol{P}_{\mathrm{A}} + \boldsymbol{P}_{\mathrm{B}}\right), \tag{6}$$

where $\boldsymbol{P}_{\mathrm{A}}$, $\boldsymbol{P}_{\mathrm{B}}$, and $\boldsymbol{P}_{\mathrm{C}}$ are the lab-frame momenta and the reduced mass associated with $\boldsymbol{\rho}_{\mathrm{AB,C}}$ is

$$\frac{1}{\mu_{\mathrm{AB,C}}} = \frac{1}{m_{\mathrm{AB}}} + \frac{1}{m_{\mathrm{C}}}. \tag{7}$$

Similarly, the conjugate momentum of $\boldsymbol{\rho}_{\mathrm{AB}}$ is

$$\boldsymbol{p}_{\mathrm{AB}} = \mu_{\mathrm{AB}}\,\dot{\boldsymbol{\rho}}_{\mathrm{AB}} = \mu_{\mathrm{AB}}\left(\frac{\boldsymbol{P}_{\mathrm{B}}}{m_{\mathrm{B}}} - \frac{\boldsymbol{P}_{\mathrm{A}}}{m_{\mathrm{A}}}\right), \tag{8}$$

where the reduced mass is

$$\frac{1}{\mu_{\mathrm{AB}}} = \frac{1}{m_{\mathrm{A}}} + \frac{1}{m_{\mathrm{B}}}. \tag{9}$$

The momentum of the ABC parent molecule is

$$\boldsymbol{p}_{\mathrm{ABC}} = M\dot{\boldsymbol{X}} = \boldsymbol{P}_{\mathrm{A}} + \boldsymbol{P}_{\mathrm{B}} + \boldsymbol{P}_{\mathrm{C}}. \tag{10}$$

Since in the experiment we evaluate the momenta of all fragments in the parent molecule's CM frame, i.e., $\boldsymbol{p}_{\mathrm{ABC}} = 0$, Eq. (6) simplifies to

$$\boldsymbol{p}_{\mathrm{AB,C}} = \boldsymbol{P}_{C}. \tag{11}$$

Finally, we define the angle $\theta_{\mathrm{AB,C}}$ between $\boldsymbol{p}_{\mathrm{AB,C}}$ and $\boldsymbol{p}_{\mathrm{AB}}$, shown in Fig. 2(b), as

$$\theta_{\mathrm{AB,C}} = \cos^{-1}\left(\frac{\boldsymbol{p}_{\mathrm{AB,C}}\cdot\boldsymbol{p}_{\mathrm{AB}}}{|\boldsymbol{p}_{\mathrm{AB,C}}|\,|\boldsymbol{p}_{\mathrm{AB}}|}\right). \tag{12}$$

It is important to note that to analyze sequential breakup via a different intermediate, one still uses the same approach detailed above, but must choose the initial Jacobi set of specific interest. In the case of three-body breakup, there are three possible choices for the Jacobi sets. In addition, the A, B, and C fragments may also represent molecular fragments. In this case, their corresponding momentum, e.g. $\boldsymbol{P}_{\mathrm{A}}$, corresponds to the center-of-mass momentum of the molecular fragment.

B. Signature of sequential fragmentation

The key to identifying sequential breakup and then separating it from concerted fragmentation is a clear signature, which in this case is the rotation of the intermediate AB molecule in the fragmentation plane. To clearly identify this signature of sequential fragmentation, the following two conditions must be valid:

1. The rotation of $\boldsymbol{p}_{\mathrm{AB}}$ occurs in the fragmentation plane, with a normal vector defined by $\boldsymbol{p}_{\mathrm{AB}}\times\boldsymbol{p}_{\mathrm{AB,C}}$.

2. AB rotates long enough to "forget" its initial alignment with respect to the first fragmentation step given by $\boldsymbol{p}_{\mathrm{AB,C}}$.

When both conditions are satisfied, the signature of sequential fragmentation is a nearly uniform $N(\theta_{\mathrm{AB,C}})$ distribution, while concerted breakup is expected to be peaked about some $\theta_{\mathrm{AB,C}}$. In Appendix A, we introduce a simple model explaining why the $N(\theta_{\mathrm{AB,C}})$ distribution is not exactly uniform.

Another way to phrase the first condition is that the angular momentum of the AB intermediate, i.e., $\boldsymbol{J}_{\mathrm{AB}}$, is parallel to the normal of the fragmentation plane. In the case of a bent triatomic molecule, all the atomic constituents must lie in the molecular plane. Therefore, using classical arguments and assuming central forces, the interaction between the C fragment and the intermediate AB molecule produces a torque, and hence angular momentum $\boldsymbol{J}_{\mathrm{AB}}$ about the CM of AB, that is perpendicular to the molecular plane. As long as the mechanisms for producing a component of angular momentum within the molecular plane are minor, then the AB intermediate should rotate mostly within the fragmentation plane. Some examples of mechanisms that may induce angular momentum within the molecular plane are forces due to the electrons ejected during ionization, an asymmetric electron charge distribution above and below the molecular plane due to the interference of opposite parity states, or initial angular momentum due to the temperature of the target gas. Similar arguments are also expected to apply to (nearly) planar polyatomic molecules as long as the deformations out of the molecular plane before and/or during the fragmentation are small. In contrast, the first condition is unlikely to be satisfied for non-planar polyatomic molecules, which we hope to address in the future.

If the first condition is not met, the signature of sequential fragmentation changes. One extreme example is when the conjugate momentum describing the second step, $\boldsymbol{p}_{\mathrm{AB}}$, rotates in the plane perpendicular to $\boldsymbol{p}_{\mathrm{AB,C}}$—or, equivalently, the coordinate $\boldsymbol{\rho}_{\mathrm{AB}}$ rotates in the plane perpendicular to $\boldsymbol{\rho}_{\mathrm{AB,C}}$. It may be easier to visualize this motion in real space where $\boldsymbol{\rho}_{\mathrm{AB}}$ rotates in a plane perpendicular to $\boldsymbol{\rho}_{\mathrm{AB,C}}$. In this situation, all sequential fragmentation events are peaked at $\theta_{\mathrm{AB,C}} = 90°$ instead of forming a uniform $N(\theta_{\mathrm{AB,C}})$ distribution. Similarly, the common signatures of sequential fragmentation in Dalitz plots and Newton diagrams also change.

Even though we observe a nearly uniform $N(\theta_{\mathrm{AB,C}})$ distribution in the experiment presented in this paper, the exact criteria needed to satisfy the second condition are still under investigation. Specifically, in the future we plan to determine the relationship between the rotational period of the AB intermediate and the populated state's lifetime needed to produce a uniform distribution. Intuitively, we expect a uniform $N(\theta_{\mathrm{AB,C}})$ distribution when the lifetime, τ, of the populated metastable state of the intermediate AB molecule is much longer than its rotational period T_R, i.e., $T_R \ll \tau$. We are still investigating the exact circumstances needed to produce a uniform $N(\theta_{\mathrm{AB,C}})$ distribution in general.

To further distinguish sequential from concerted breakup, we plot the three-body breakup events as a function of $\theta_{\mathrm{AB,C}}$ and the kinetic energy release (KER) in the second step, $\mathrm{KER}_{\mathrm{AB}}$, which is

$$\mathrm{KER}_{\mathrm{AB}} = \frac{\boldsymbol{p}_{\mathrm{AB}}^2}{2\mu_{\mathrm{AB}}}. \tag{13}$$

Since the internal energy of the intermediate AB molecule is independent of its final breakup angle $\theta_{\mathrm{AB,C}}$, $\mathrm{KER}_{\mathrm{AB}}$ is as well. Therefore, using the $N(\mathrm{KER}_{\mathrm{AB}}, \theta_{\mathrm{AB,C}})$ distribution is a more differential and therefore a better test for identifying and further separating sequential breakup from other processes compared to the one-dimensional $N(\theta_{\mathrm{AB,C}})$ distribution.

C. Determining the sequential fragmentation contributions in OCS

In this section, we study the three-body fragmentation of the OCS molecule using the native frames method and identify sequential fragmentation by taking advantage of its signature, i.e., the rotation of the intermediate molecule in the fragmentation plane. Before plotting the $N(\mathrm{KER}_{\mathrm{CO}}, \theta_{\mathrm{CO,S}})$ and $N(\mathrm{KER}_{\mathrm{CS}}, \theta_{\mathrm{CS,O}})$ distributions, we first discuss why the rotation of the intermediate molecule is expected to occur mostly in the fragmentation plane.

As previously stated, since OCS is a triatomic molecule, all atomic constituents lie in a well-defined molecular plane assuming the molecule is slightly bent from its linear equilibrium geometry. In the case of sequential fragmentation involving a CO^{2+} intermediate, the C−S bond breaks in the first step, producing S^+ and CO^{2+} fragments. In a simple classical model assuming central forces, the charged S^+ then interacts with point charges placed on the C and O constituents of the CO^{2+} molecule producing a torque, resulting in angular momentum perpendicular to the molecular plane. We describe such a model in App. B. Briefly, we choose the charges on C and O to reproduce the dication's ground-state dipole moment. The interaction between the S^+ and this simplified charge distribution leads to a rotation of the CO^{2+} in the plane, leading to more than $20\hbar$ of angular momentum even for bending angles only a couple of degrees from linear. For similar reasons, the rotation of the CS^{2+} intermediate should occur in the fragmentation plane as well.

To identify sequential fragmentation involving the CO^{2+} intermediate, we plot the $N(\mathrm{KER}_{\mathrm{CO}}, \theta_{\mathrm{CO,S}})$ distribution for all events, shown in Fig. 3(a), where a uniform $N(\theta_{\mathrm{CO,S}})$ distribution appears for $\theta_{\mathrm{CO,S}} \lesssim 60°$ centered at a $\mathrm{KER}_{\mathrm{CO}} \sim 6.5\,\mathrm{eV}$. The $N(\theta_{\mathrm{CO,S}})$ distribution integrated over all $\mathrm{KER}_{\mathrm{CO}}$, shown in Fig. 3(b), emphasizes that the distribution is uniform for $\theta_{\mathrm{CO,S}} \lesssim 60°$. Only a subset of $\theta_{\mathrm{CO,S}}$ displays a uniform distribution since other competing processes, such as concerted breakup, overlap the sequential fragmentation events and create a peak, visible at $\theta_{\mathrm{CO,S}} \sim 120°$. To show that the uniform

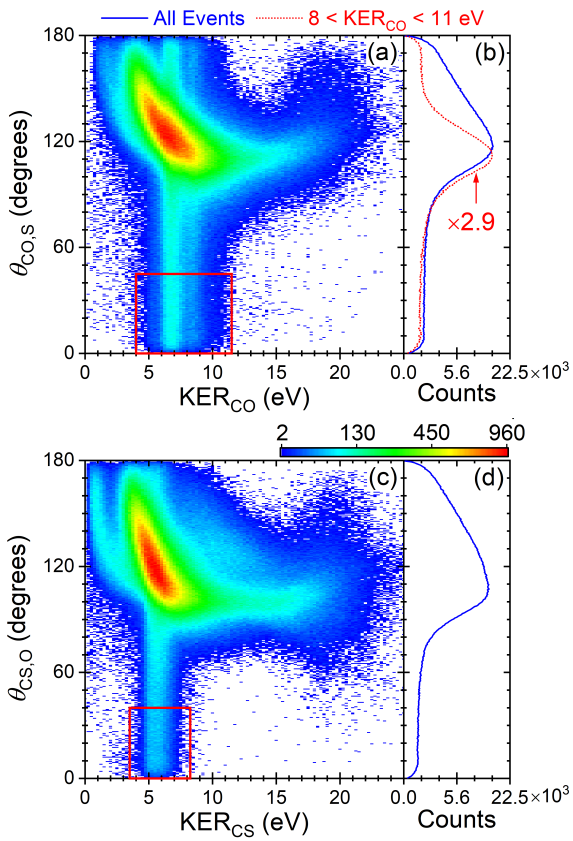

FIG. 3. (Color online) All $O^+ + C^+ + S^+$ events as a function of (a) $\mathrm{KER_{CO}}$ and $\theta_{\mathrm{CO,S}}$, (b) $\theta_{\mathrm{CO,S}}$, (c) $\mathrm{KER_{CS}}$ and $\theta_{\mathrm{CS,O}}$, and (d) $\theta_{\mathrm{CS,O}}$. The $N(\theta_{\mathrm{CO,S}})$ distributions in (b) are integrated over all $\mathrm{KER_{CO}}$ (blue-solid curve) and the higher energy slice of the sequential breakup (see text) $8 \leq \mathrm{KER_{CO}} \leq 11$ eV (red-dot curve), while the $N(\theta_{\mathrm{CS,O}})$ distribution in (d) is integrated over all $\mathrm{KER_{CS}}$ (blue-solid curve). Note that the error bars of the $N(\theta_{\mathrm{CO,S}})$ and $N(\theta_{\mathrm{CS,O}})$ distributions appear as shaded regions, which is the style used throughout this paper. In this figure, the error bars are approximately the thickness of the line. The red rectangles define the regions used in Sec. IV to select sequential fragmentation events.

distribution reemerges from the competing processes at large angles, in Fig. 3(b) we also plot the $N(\theta_{\mathrm{CO,S}})$ distribution integrated over the higher $\mathrm{KER_{CO}}$ part of the sequential breakup involving CO^{2+} intermediate, namely $8 < \mathrm{KER_{CO}} < 11\,\mathrm{eV}$, which is uniform for $\theta_{\mathrm{CS,O}} > 150°$ as well.

To determine if sequential fragmentation involving the CS^{2+} intermediate occurs, we plot in Figs. 3(c) and (d), respectively, the $N(\mathrm{KER_{CS}}, \theta_{\mathrm{CS,O}})$ and $N(\theta_{\mathrm{CS,O}})$ distributions for all events. In these plots, we identify sequential fragmentation as a uniform $N(\theta_{\mathrm{CS,O}})$ distribution for $\theta_{\mathrm{CS,O}} \lesssim 60°$ centered at $\mathrm{KER_{CS}} \sim 5.5\,\mathrm{eV}$. Later, in Sec. VI A, we show that sequential fragmentation involving the CO^{2+} fragment and concerted breakup both contribute in forming a peak at $\theta_{\mathrm{CS,O}} \sim 110°$.

Unfortunately, the $N(\theta_{\mathrm{CO,S}})$ and $N(\theta_{\mathrm{CS,O}})$ distributions, shown in Fig. 3, are not perfectly uniform, with "dips" occurring at 0° and 180°. One possible source of the dips is purely geometrical, as a consequence of using a polar angle $\theta_{\mathrm{AB,C}}$ to describe the rotation of the AB intermediate, which forms a uniform distribution in a ring with finite thickness, as we explain further in Appendix A. However, an experimental artifact due to the reduced efficiency near the center of the position sensitive detector may also contribute to these dips. Specifically, the lower efficiency region on the detector is caused by the high rate of OCS^{q+} molecules and He ions from the carrier gas. In the case of sequential fragmentation via a CO^{2+} intermediate, the O^+ fragment has a small kinetic energy when $\theta_{\mathrm{CO,S}} = 0°$ because it is ejected in the opposite direction of the CO^{2+} molecule's center-of-mass. On the other hand, the C^+ fragment has a similarly small kinetic energy when $\theta_{\mathrm{CO,S}} = 180°$. As a result, these fragments do not have enough momentum parallel to the detector plane to escape the inefficient detector regions regardless of the laser's polarization direction, potentially contributing to the dips at the edges of the $N(\theta_{\mathrm{CO,S}})$ distribution. Fortunately, since the dips only affect a small part of the $N(\theta_{\mathrm{CO,S}})$ and $N(\theta_{\mathrm{CS,O}})$ distributions, the native-frames method can still be applied.

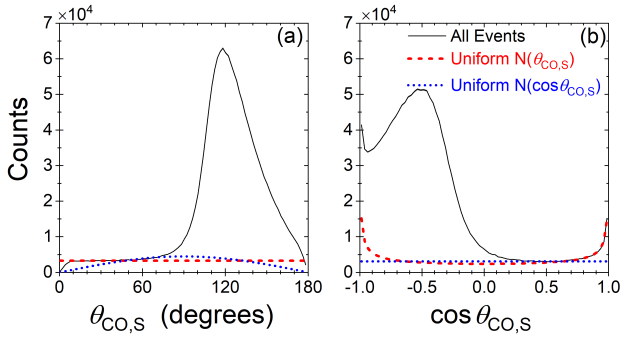

FIG. 4. (Color online) All $O^+ + C^+ + S^+$ events plotted in black as a function of (a) $\theta_{\mathrm{CO,S}}$ and (b) $\cos\theta_{\mathrm{CO,S}}$. In addition, the red and blue lines show the functional forms of uniform $N(\theta_{\mathrm{CO,S}})$ and $N(\cos\theta_{\mathrm{CO,S}})$ distributions, respectively (see text). Clearly, the data follow the $N(\theta_{\mathrm{CO,S}})$ distribution more closely than the $N(\cos\theta_{\mathrm{CO,S}})$ distribution for $\theta_{\mathrm{CO,S}} \sim 0$.

A valid question to ask is why sequential fragmentation is uniform in $\theta_{\mathrm{AB,C}}$ instead of $\cos\theta_{\mathrm{AB,C}}$ since $\theta_{\mathrm{AB,C}}$ is a polar angle in the body-fixed frame, shown in Fig. 2(b). In general, three-dimensional distributions are plotted as a function of $\cos\theta$ since isotropic spherical distributions produce a uniform $N(\cos\theta)$ distribution. In the case of sequential fragmentation, the conjugate momentum corresponding to the second fragmentation step, $\boldsymbol{p}_{\mathrm{AB}}$, predominantly rotates in a plane, producing a uniform angular distribution along a ring instead of a sphere. Therefore, we plot $\theta_{\mathrm{AB,C}}$ instead of $\cos\theta_{\mathrm{AB,C}}$ (see Appendix A).

To demonstrate this point, we plot the $N(\theta_{\mathrm{CO,S}})$ and $N(\cos\theta_{\mathrm{CO,S}})$ distributions for all events in Fig. 4(a) and Fig. 4(b), respectively. In addition, we plot the func-

tional forms of uniform distributions in $N(\theta_{\mathrm{CO,S}})$ and $N(\cos\theta_{\mathrm{CO,S}})$ (red and blue dotted lines, respectively). In Fig. 4(a), the uniform $N(\theta_{\mathrm{CO,S}})$ distribution fits the data nicely, while the uniform $N(\cos\theta_{\mathrm{CO,S}})$ distribution does not [85]. Similarly, Fig.4(b) shows that the uniform $N(\theta_{\mathrm{CO,S}})$ distribution fits the data best [86].

Therefore, in the case of the sequential three-body fragmentation of the OCS molecule into $O^+ + C^+ + S^+$, the signature of sequential fragmentation via the CO^{2+} and CS^{2+} intermediates are uniform $N(\theta_{\mathrm{CO,S}})$ and $N(\theta_{\mathrm{CS,O}})$ distributions, respectively.

D. Euler angle analysis

In this section, we perform additional analysis to study the alignment of the fragmentation plane in space using Euler angles for the events contributing to sequential breakup. In particular, we expect that the $N(\theta_{\mathrm{AB,C}})$ distribution should be uniform for any orientation of the fragmentation plane in space since the mechanism given for acquiring angular momentum does not depend on the Euler angle.

To define the Euler angles, we begin with the lab-fixed XYZ coordinate system, where we fix the $\hat{\boldsymbol{Z}}$ axis along the laser polarization, the $\hat{\boldsymbol{Y}}$ axis is parallel to the laser propagation direction, and $\hat{\boldsymbol{X}}$ is chosen to form a right-handed coordinate system. Additionally, we define the body-fixed xyz axes for sequential breakup involving the intermediate AB molecule, shown in Fig. 5(d), as

$$\hat{\boldsymbol{z}}_{\mathrm{AB}} = \frac{\boldsymbol{p}_{\mathrm{AB,C}} \times \boldsymbol{p}_{\mathrm{AB}}}{\left|\boldsymbol{p}_{\mathrm{AB,C}} \times \boldsymbol{p}_{\mathrm{AB}}\right|}, \tag{14}$$

which is the normal of the fragmentation plane, while the axes within the plane are

$$\hat{\boldsymbol{y}}_{\mathrm{AB}} = \frac{\boldsymbol{p}_{\mathrm{AB,C}}}{\left|\boldsymbol{p}_{\mathrm{AB,C}}\right|}, \tag{15}$$

and

$$\hat{\boldsymbol{x}}_{\mathrm{AB}} = \frac{\hat{\boldsymbol{y}}_{\mathrm{AB}} \times \hat{\boldsymbol{z}}_{\mathrm{AB}}}{\left|\hat{\boldsymbol{y}}_{\mathrm{AB}} \times \hat{\boldsymbol{z}}_{\mathrm{AB}}\right|}. \tag{16}$$

The Euler angles α_{AB}, β_{AB}, and γ_{AB} are shown pictorially in Fig. 5(d). The angle α_{AB} is defined as

$$\alpha_{\mathrm{AB}} = \tan^{-1}\left(-\frac{\hat{\boldsymbol{N}}_{\mathrm{AB}} \cdot \hat{\boldsymbol{X}}}{\hat{\boldsymbol{N}}_{\mathrm{AB}} \cdot \hat{\boldsymbol{Y}}}\right), \tag{17}$$

where the line of nodes $\hat{\boldsymbol{N}}_{\mathrm{AB}}$ is

$$\hat{\boldsymbol{N}}_{\mathrm{AB}} = \frac{\hat{\boldsymbol{Z}} \times \hat{\boldsymbol{z}}_{\mathrm{AB}}}{\left|\hat{\boldsymbol{Z}} \times \hat{\boldsymbol{z}}_{\mathrm{AB}}\right|}. \tag{18}$$

Physically, α_{AB} is the angle between $\hat{N}_{\mathrm{AB}}$ (the intersection between the xy and XY planes) and the Y axis. Given that $\hat{N}_{\mathrm{AB}}$ is always perpendicular to the projection of z_{AB} into the XY plane, α_{AB} represents the azimuthal angle of z_{AB} about the laser polarization (Z axis). Because we have a linearly-polarized field, L_Z is conserved. Consequently, the $N(\alpha_{\mathrm{AB}})$ distribution should be uniform. The angle β_{AB} is the angle between the normal to the fragmentation plane and the laser polarization given by

$$\cos\beta_{\mathrm{AB}} = \hat{\boldsymbol{Z}} \cdot \hat{\boldsymbol{z}}_{\mathrm{AB}}. \tag{19}$$

Finally, γ_{AB} is

$$\gamma_{\mathrm{AB}} = \tan^{-1}\left(\frac{\hat{\boldsymbol{N}}_{\mathrm{AB}} \cdot \hat{\boldsymbol{x}}_{\mathrm{AB}}}{\hat{\boldsymbol{N}}_{\mathrm{AB}} \cdot \hat{\boldsymbol{y}}_{\mathrm{AB}}}\right). \tag{20}$$

where $\boldsymbol{p}_{\mathrm{AB,C}}$ lies along the projection of the laser polarization into the fragmentation plane when $\gamma_{\mathrm{AB}} = \pm 90°$. In other words, γ_{AB} provides information about the relative angle between $\boldsymbol{p}_{\mathrm{AB,C}}$ and the projection of the laser polarization into the fragmentation plane.

In Fig. 5(a-c), we show density plots of all $O^+ + C^+ + S^+$ events as a function of the individual Euler angles and $\theta_{\mathrm{CO,S}}$, the angle related to the rotation of the intermediate CO^{2+} in the native frames analysis. Note that in each plot, we integrate over all other degrees of freedom not shown in the figure, such as the remaining Euler angles and KER. To demonstrate that sequential fragmentation involving the CO^{2+} intermediate produces a uniform $N(\theta_{\mathrm{CO,S}})$ distribution for any spatial orientation of the fragmentation plane, we must recall that sequential breakup is only separated for $\theta_{\mathrm{CO,S}} \lesssim 60°$ while larger angles also contain other competing processes. Therefore, we only expect the $N(\alpha_{\mathrm{CO}}, \theta_{\mathrm{CO,S}})$, $N(\cos\beta_{\mathrm{CO}}, \theta_{\mathrm{CO,S}})$, and $N(\gamma_{\mathrm{CO}}, \theta_{\mathrm{CO,S}})$ distributions, shown in Fig. 5(a-c), to be uniform for $\theta_{\mathrm{CO,S}} \lesssim 60°$.

The density plots of all $O^+ + C^+ + S^+$ events as a function of the Euler angles and $\theta_{\mathrm{CS,O}}$ similarly show that sequential fragmentation involving the CS^{2+} intermediate's $N(\theta_{\mathrm{CS,O}})$ distribution is uniform for any fragmentation plane's orientation in space, as shown in Fig. 5(e-f) for $\theta_{\mathrm{CS,O}} \lesssim 60°$. Note that we do not plot $N(\alpha_{\mathrm{CS}}, \theta_{\mathrm{CS,O}})$, which yields a nearly identical plot to Fig. 5(a), because of the same symmetry argument used for $N(\alpha_{\mathrm{CO}}, \theta_{\mathrm{CO,S}})$ above.

The Euler angles also contain information about the spatial alignment of the sequential fragmentation events. For example, the $N(\cos\beta_{\mathrm{CO}}, \theta_{\mathrm{CO,S}})$ and $N(\cos\beta_{\mathrm{CS}}, \theta_{\mathrm{CS,O}})$ distributions for sequential breakup (at $\theta_{\mathrm{AB,C}} \leq 60°$), shown in Fig. 5(b) and Fig. 5(e), respectively, demonstrate that the laser polarization is preferentially within the fragmentation plane since both distributions are peaked at $\cos\beta = 0$. Additionally, the $N(\gamma_{\mathrm{CO}})$ and $N(\gamma_{\mathrm{CS}})$ distributions, shown in Fig. 5(c) and Fig. 5(f), respectively, show that the first step of sequential fragmentation (again, at angles $\theta_{\mathrm{AB,C}} \leq 60°$) tends to roughly align along the projection of the polarization

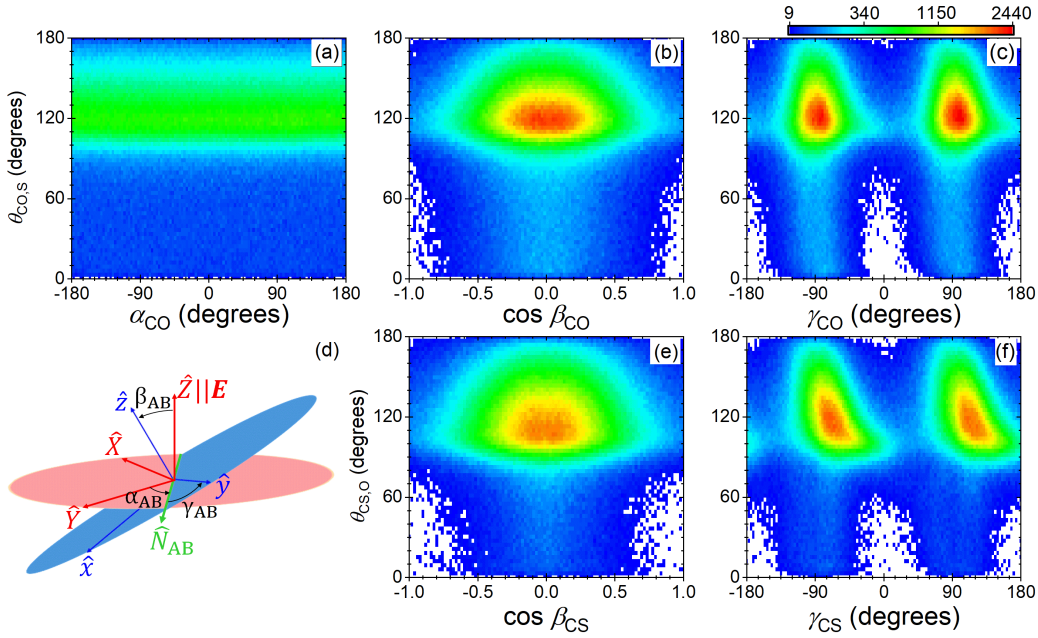

FIG. 5. (Color online) All $O^+ + C^+ + S^+$ events as a function of (a) α_{CO} and $\theta_{CO,S}$, (b) $\cos\beta_{CO}$ and $\theta_{CO,S}$, and (c) γ_{CO} and $\theta_{CO,S}$, which represent the alignment of the fragmentation plane for sequential fragmentation via the CO^{2+} intermediate. (d) A schematic displaying the Euler angles for sequential fragmentation via an arbitrary AB molecule. All $O^+ + C^+ + S^+$ events as a function of (e) $\cos\beta_{CS}$ and $\theta_{CS,O}$, and (f) γ_{CS} and $\theta_{CS,O}$ for sequential fragmentation involving the CS^{2+} intermediate.

axis ($\hat{\boldsymbol{Z}}$) into the fragmentation plane since the distributions are peaked at $\gamma = \pm 90°$.

Finally, we demonstrate (in Sec. VI D) the use of the Euler angles distributions, in conjunction with other aspects of the native-frames method, to exclude sequential fragmentation via the SO^{2+} intermediate in our experiment.

IV. UNDERSTANDING SEQUENTIAL FRAGMENTATION

Having identified sequential fragmentation, we can extract information about the first and second fragmentation steps of the sequential breakup, such as the kinetic energy released in each step, as well as determine the branching ratios of sequential versus concerted breakup. We discuss how to retrieve such information in the following section.

A. Sequential fragmentation – first step

Here, we compare the first step of sequential three-body fragmentation via the CO^{2+} and CS^{2+} intermediate molecules to the two-body $CO^{2+} + S^+$ and $CS^{2+} + O^+$ breakup channels, respectively. The motivation behind this comparison is the assessment that two-body breakup, via $CO^{2+} + S^+$ and $CS^{2+} + O^+$, is similar to the first step in sequential three-body fragmentation, but the intermediate dication survives intact all the way to the detector. By contrasting the KER distributions, we learn about the differences between the populated states leading to each outcome.

Returning to the ABC notation, the KER of the first fragmentation step is

$$\mathrm{KER}_{\mathrm{AB,C}} = \frac{\boldsymbol{p}^2_{\mathrm{AB,C}}}{2\mu_{\mathrm{AB,C}}}. \tag{21}$$

In addition, the angle θ of the first-step conjugate momentum with respect to the laser polarization, $\hat{\boldsymbol{Z}}$, is

$$\cos\theta = \frac{\boldsymbol{p}_{\mathrm{AB,C}} \cdot \hat{\boldsymbol{Z}}}{|\boldsymbol{p}_{\mathrm{AB,C}}|}. \tag{22}$$

The $N(\mathrm{KER}_{\mathrm{AB,C}}, \cos\theta)$ distributions for the three-body sequential fragmentation channels involving the intermediate CO^{2+} and CS^{2+} molecules are shown in Fig. 6(a) and Fig. 6(b), respectively. Note that to make these plots, we select the sequential fragmentation events in the regions marked by red rectangles in Fig. 3, where $\theta_{CO,S} \leq 45$ and $\theta_{CS,O} \leq 40°$ for the CO^{2+} and CS^{2+} intermediate molecules, respectively. For comparison, the distributions of the two-body breakup channels, $CO^{2+} + S^+$ and $CS^{2+} + O^+$, are presented in Fig. 6(c) and Fig. 6(d), respectively. The associated $\mathrm{KER}_{\mathrm{AB,C}}$ distributions integrated over all other degrees of freedom are

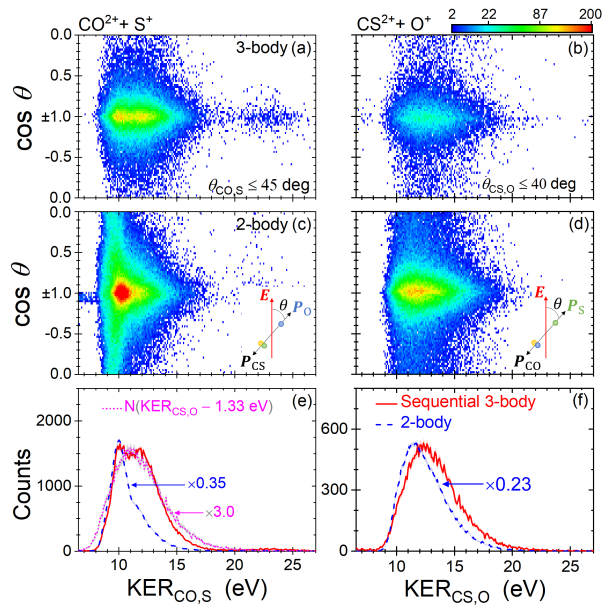

FIG. 6. (Color online) Sequential fragmentation events via $CO^{2+}+S^{+}$ (left column) and $CS^{2+}+O^{+}$ (right column) plotted as a function of (a) $KER_{CO,S}$ and $\cos\theta$, and (b) $KER_{CS,O}$ and $\cos\theta$ for the regions $\theta_{CO,S} \leq 45$ and $\theta_{CS,O} \leq 40^{\circ}$, respectively. The angle θ is defined in Eq. 22. The two-body fragmentation via $CO^{2+}+S^{+}$ and $CS^{2+}+O^{+}$, associated with their respective sequential breakup, as a function of (c) $KER_{CO,S}$ and $\cos\theta$, and (d) $KER_{CS,O}$ and $\cos\theta$, respectively. The (e) $N(KER_{CO,S})$ and (f) $N(KER_{CS,O})$ distributions integrated over $\cos\theta$.

shown in Fig. 6(e-f). The three-body and two-body distributions look similar, especially the angular distributions that exhibit a strong alignment preference along the laser polarization.

One notable difference is that the three-body sequential breakup extends to higher KER than the two-body breakup, as indicated by Fig. 6(e-f), especially for the $CO^{2+}+S^{+}$ channel. This KER measures the energy difference between the OCS^{3+} state populated by triple ionization and the $CO^{2+}+S^{+}$ [or $CS^{2+}+O^{+}$] dissociation limit (note that these dissociation limits are bands in energy because of the internal, rovibrational, energy of the intact intermediate). Given that the internal energy spread of the CO^{2+} states that survive all the way to the detector is small, i.e., less than 0.23 eV [87–89] (0.52 eV for CS^{2+} [90]), the dissociation-limit spread is too small to cause the difference in the $KER_{CO,S}$ distributions observed in Fig. 6(e). Therefore, we expect higher electronic states of OCS^{3+} to be responsible for the higher KER tail in the sequential three-body breakup.

In addition, careful inspection of Fig. 6(e-f) indicates that the $KER_{CS,O}$ distribution is shifted up with respect to the $KER_{CO,S}$ distribution by about 1.3 eV. This energy shift matches the difference between the dissociation limits of the $CO^{2+}+S^{+}$ and $CS^{2+}+O^{+}$ channels in their lowest rovibrational state of the ground $X^{3}\Pi$ electronic

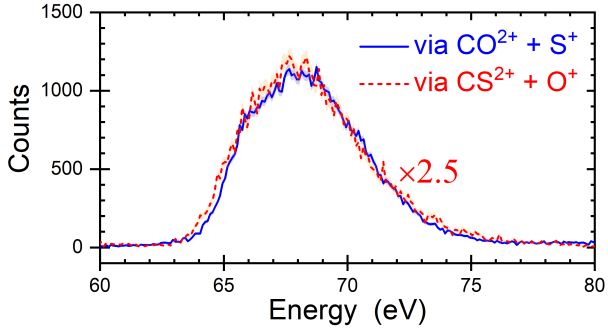

FIG. 7. (Color online) The energy distributions of sequential three-body fragmentation via the CO^{2+} and CS^{2+} intermediates. We select the relevant event using the, respective, $\theta_{CO,S} \leq 45^{\circ}$ and $\theta_{CS,O} \leq 40^{\circ}$ conditions. Zero energy is set at the ground state, $X\,^{1}\Sigma^{+}(v{=}0,0,0)$, of the OCS molecule.

state [90, 91]. This suggests that each sequential fragmentation pathway leading to $O^{+}+C^{+}+S^{+}$ may originate at the same energy on the potential energy surfaces of the transient OCS^{3+} molecule, but break along different reaction coordinates.

To further explore this point, we plot the energy of the sequential three-body breakup in Fig. 7, where $E=0$ represents the energy of the ground $X\,^{1}\Sigma^{+}(v{=}0,0,0)$ state of the neutral OCS molecule. The energy scale in Fig. 7 is equivalent to the one used in the potential energy plots reported by Eland *et al.* [92], allowing us to determine which OCS^{3+} states contribute. Assuming that the fragmentation ends on the lowest dissociation limit of $O^{+}+C^{+}+S^{+}$, we compute the excitation energy with respect to the OCS ground state, $X\,^{1}\Sigma^{+}(v{=}0,0,0)$, by summing the KER, the ionization energies of each atomic fragment [93], and the dissociation energies of the $OCS(X\,^{1}\Sigma^{+})$ ground state into $CO(X\,^{1}\Sigma^{+}(v{=}0))+S(^{3}P)$ [94] and $CO(X\,^{1}\Sigma^{+}(v{=}0))$ into $C(^{3}P)+O(^{3}P)$ [95]. Here, and throughout the manuscript, the atomic-states labels are the lowest of each symmetry and they are associated with the dissociation limits as shown in Figs. 8 and 9. Note that the KER mentioned above is given by

$$\mathrm{KER} = \mathrm{KER}_{\mathrm{AB,C}} + \mathrm{KER}_{\mathrm{AB}}, \tag{23}$$

i.e., the energy release in the two fragmentation steps.

In Fig. 7, we see that the energy distributions for both three-body sequential processes overlap, reinforcing the idea that both sequential breakup processes begin on the same group of potential energy surfaces. Then, asymmetric stretching of the O–C or C–S bond on each potential surface is required to form a CS^{2+} or CO^{2+} intermediate, respectively, in the first step. We note that the OCS^{3+} electronic ground state is about ∼61 eV above the OCS ground state at the equilibrium geometry [92]. This energy is significantly lower than the energy evaluated from our measured KER, shown in Fig. 7, suggesting that the OCS^{3+} ground state does not contribute significantly to the sequential breakup in our measurements.

On the other hand, the measured energy distribution, and in particular its width, are consistent with contributions from a group of low-lying excited states of OCS^{3+}, which span 4−15 eV above its electronic ground state (see Table I in Ref. [92]). In the interpretation above we assumed that multi-photon ionization lands the OCS^{3+} on the potential surfaces, while the electrons carry the excess energy. The validity of these assumptions as well as the relative importance of each of these states and their specific energy spectrum requires theoretical treatment that is beyond the scope of our work.

B. Sequential fragmentation – second step

Plots of the second-step KER distribution, i.e., $N(\mathrm{KER_{AB}})$, are useful for determining the internal energy of the metastable AB intermediate. In Fig. 8(a), we show the $N(\mathrm{KER_{AB}})$ distribution for $\theta_{\mathrm{CO,S}} \leq 45°$, which only contains sequential fragmentation events involving the CO^{2+} intermediate. In addition, we include tick marks representing the expected $\mathrm{KER_{CO}}$ associated with field-free vibrational states of the four lowest electronic states of CO^{2+} for $J = 1$. Aside from the lower comb of $A^3\Sigma^+$ vibrational states, the calculation of the $\mathrm{KER_{CO}}$ of each vibrational state assumes predissociation to the lowest asymptotic limit of CO^{2+}. For example, one possible pathway from the $A^3\Sigma^+$ state is via spin-orbit coupling to the repulsive $^3\Sigma^-$ state. In contrast, the lower comb of $A^3\Sigma^+$ vibrational states assumes fragmentation leading to the first excited $C^+(^2P) + O^+(^2D)$ dissociation limit, which can occur via spin-orbit coupling through the $c\,^1\Delta$ state.

For an electronic state to contribute to the measured $N(\mathrm{KER_{CO}})$ distribution, the rovibrational state's lifetime must fall within a certain time window. The upper limit is related to the flight time of the CO^{2+} and CS^{2+} intermediate molecules to the detector, which in our experiment is approximately 3 μs. Using momentum conservation, we can exclude events in which the intermediate molecule, CO^{2+} for example, moves significantly in the spectrometer before dissociating. We estimate that such events involving CO^{2+} dissociation in flight can be separated if the flight time is longer than 200 ns. Therefore, contributions from states with longer lifetimes will be significantly suppressed. For example, only 5 % of the population of a state with $\tau = 3\,\mu$s may contribute to the $N(\mathrm{KER_{CO}})$ distribution.

On the other hand, the lowest lifetime depends on the ratio between the intermediate molecule's rotational period, T_R, and τ. If $T_R \ll \tau$, then we expect to observe a uniform $N(\theta_{\mathrm{AB,C}})$ distribution as long as the rotation occurs in the fragmentation plane. The exact relationship between T_R and τ needed to produce a uniform $N(\theta_{\mathrm{AB,C}})$ distribution is still under investigation. Assuming a rigid-rotor, the rotational period decreases with increasing angular momentum. For example, if $J = 20$, $T_R \approx 550$ fs for the ground $X^3\Pi(v{=}0)$ state, as compared to $T_R \approx 8$ ps for $J = 1$. This suggests that states with higher J and lifetimes of several hundreds of femtoseconds to a few picoseconds can contribute to the measured $N(\mathrm{KER_{CO}})$ distributions.

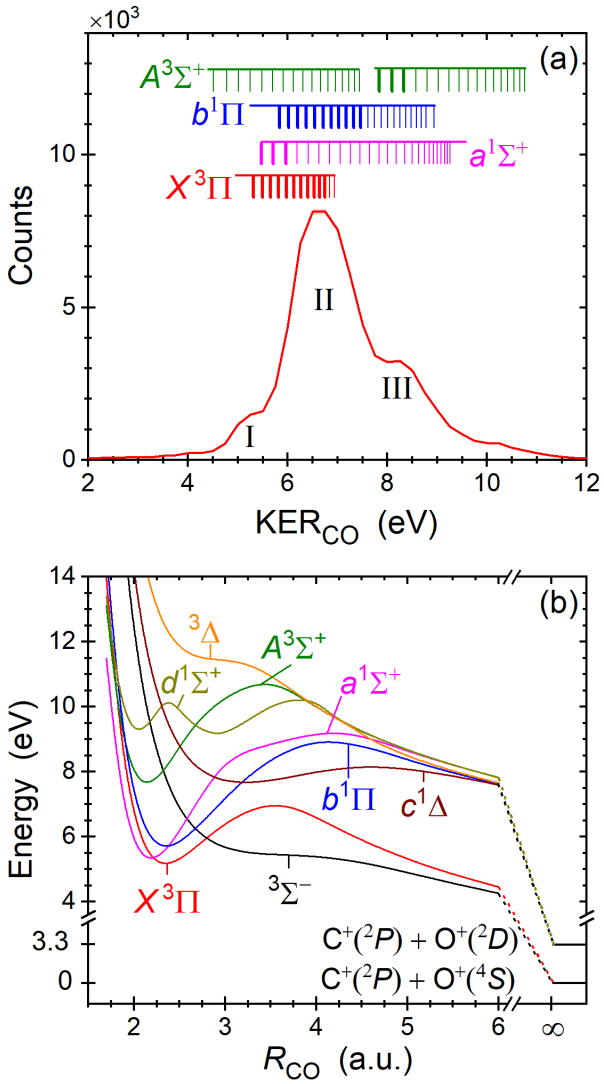

FIG. 8. (Color online) (a) Sequential fragmentation events via the CO^{2+} intermediate as a function of $\mathrm{KER_{CO}}$ for $\theta_{\mathrm{CO,S}} \leq 45°$. The expected field-free KER of the vibrational states of the four lowest lying electronic states are depicted by the tick marks. Specifically, the thick tick marks are based on high-resolution spectroscopy by Lundqvist *et al.* [88] with the assignment correction noted by Hochlaf *et al.* [89]. For the low-lying states not measured in the previous experiments [88, 89], the vertical photoionization energies provided by Dawber *et al.* [96] are used. The thin tick marks are calculated using the phase amplitude method [97] for $J = 1$ and the potential energy curves provided in Ref. [91]. (b) The potential energy curves of CO^{2+} (adapted from Ref. [91]).

For the sake of discussing which rovibrational states may contribute to the $N(\mathrm{KER_{CO}})$ distribution, we limit the discussion to $J = 1$ ($T_R \sim 8$ ps for $v = 0$ in the ground

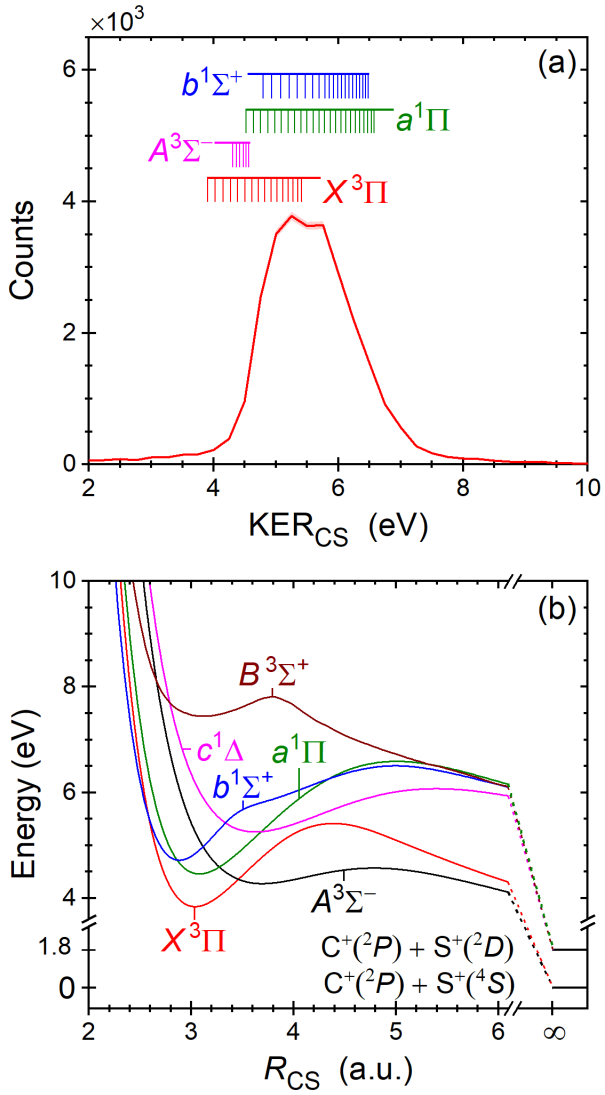

FIG. 9. (Color online) (a) Sequential fragmentation events via the CS^{2+} intermediate as a function of KER_{CS} for $\theta_{CS,O} \leq 40°$. The expected field-free KER of the vibrational states of the four lowest lying electronic states are depicted by the tick marks, which we calculated using the phase amplitude method [97] for the potential energy curves reported in Ref. [90]. (b) The potential energy curves of CS^{2+} (adapted from Ref. [90]).

$X\,^3\Pi$ state) since lifetime calculations for high J values are not readily available for the CO^{2+} and CS^{2+} molecules and predissociation lifetimes depend on J [98, 99]. Following the arguments above, the lowest vibrational level ($v=0$) of the $X\,^3\Pi$, $a\,^1\Sigma^+$ and $b\,^1\Pi$ states do not contribute to the measured $N(KER_{CO})$ distribution, since their lifetimes are significantly longer than the flight time to the detector [87, 91]. The remaining vibrational states of the $X\,^3\Pi$ and $a\,^1\Sigma^+$ states as well as the $b\,^1\Pi$ state may contribute to the dominant KER_{CO} peak, labeled II in Fig. 8(a). Curiously, the lifetimes of the $v=8$ and 9 levels of the $X\,^3\Pi$, which align well with the II KER peak in Fig. 8(a), are 98 and 22 ps, respectively, according to our calculations using the method described in Ref. [87]. Such lifetimes allow the CO^{2+} intermediate to rotate long enough to create the uniform angular distribution, while their translation in the setup is negligible. However, this statement should be taken with a grain of salt as the predissociation lifetimes of low vibrational levels vary by more than an order of magnitude across different computation methods [91]. Other rovibrational states of these electronic states may have lifetimes too short to contribute to the KER_{CO} distribution. The high-KER_{CO} peak, labeled III in Fig. 8(a), may be associated with the high-lying vibrational states of the $a\,^1\Sigma^+$ and $b\,^1\Pi$ states as well as the low-lying vibrational states of the $A\,^3\Sigma^+$ state.

To identify states responsible for the low-KER_{CO} shoulder, labeled I in Fig. 8(a), higher excited states of the CO^{2+} intermediate molecule that predissociate to the first excited $C^+(^2P) + O^+(^2D)$ limit must be considered. One possible electronic state is the $A\,^3\Sigma^+$ with vibrational states that can predissociate through spin-orbit coupling to the $c\,^1\Delta$ state, which are represented by the low KER_{CO} set of tick marks associated with the $A\,^3\Sigma^+$ state in Fig. 8(a). Higher lying vibrational states of the $a\,^1\Sigma^+$ and the $b\,^1\Pi$ may also predissociate via the $c\,^1\Delta$ state leading to energies that may contribute to the lowest KER_{CO} peak.

Similarly for fragmentation via the CS^{2+} intermediate, Fig. 9(a) shows the $N(KER_{CS})$ distribution for $\theta_{CS,O} \leq 40°$, shown as the red rectangle in Fig. 3(c). Here too, the tick marks represent the expected KER_{CS} for various vibrational and electronic states of CS^{2+} with $J=1$. Using arguments similar to those provided for the CO^{2+} intermediate and the reported lifetimes of the CS^{2+} molecule [90], we can determine the relevant states that contribute to the measured $N(KER_{CS})$ distribution. In particular, the high-lying vibrational states of $X\,^3\Pi$ and most vibrational states of the $a\,^1\Pi$ and $b\,^1\Sigma^+$ states contribute to the main KER_{CS} peak while the $A\,^3\Sigma^-$ state may only contribute to the low-energy shoulder.

C. Total kinetic energy release

In Fig. 10, we plot the total KER for all three-body breakup into $O^+ + C^+ + S^+$ as well as the separated concerted and sequential breakup contributions. From this figure, we see that concerted fragmentation is shifted to higher KER as a result of the subtraction of the sequential breakup, which peaks a few eV lower. Assuming that all these fragmentation processes dissociate to the same, lowest, energy limit, this KER difference suggests that concerted fragmentation involves higher excited states of OCS^{3+} than the states leading to sequential breakup.

In addition, we plot the energy axis on the top of Fig. 10, which is identical to the axis in Fig. 7 and the

TABLE I. The branching ratios for the sequential and concerted fragmentation processes.

Step	Sequential		Concerted	Sequential	
	$CO^{2+}+S^+$		$O^+ + C^+ + S^+$	$CS^{2+}+O^+$	
1^{st}	$19.88 \pm 0.82\%$		$69.90 \pm 0.72\%$	$10.22 \pm 0.63\%$	
	$CO^{2+}+S^+$	$O^+ + C^+ + S^+$		$O^+ + C^+ + S^+$	$CS^{2+}+O^+$
2^{nd}	$2.61 \pm 0.79\%$	$17.27 \pm 0.19\%$	$69.90 \pm 0.72\%$	$2.05 \pm 0.62\%$	$8.17 \pm 0.10\%$

potential energy plots shown in Ref. [92]. From this figure, we see that concerted fragmentation peaks above 70 eV and extends from 64 to 90 eV. The lower limit suggests that the ground electronic state of OCS^{3+}, which is about 61 eV in the Franck-Condon region [92], does not contribute significantly to concerted breakup. Unfortunately, the potential energy surfaces reported by Eland *et al.* [92] extend only up to 68 eV, while our KER data indicates the need for potentials extending to much higher energy (i.e., by more than 20 eV) in order to identify the contributing states of the transient OCS^{3+} in our intense laser pulse.

D. Branching ratios

One advantage of the native-frames method over Newton diagrams and Dalitz plots is that it allows us a straightforward way to evaluate the branching ratios of the competing concerted and sequential breakup processes by exploiting the uniform $N(\theta_{\mathrm{AB,C}})$ distribution.

Assuming that $N(\theta_{\mathrm{AB,C}})$ is uniform over all $\theta_{\mathrm{AB,C}}$, the total number of sequential fragmentation events involving an AB molecule is

$$N_{\mathrm{AB,C}} = \frac{180}{\theta_{\max} - \theta_{\min}} \sum_{\theta_{\min}}^{\theta_{\max}} N(\theta_{\mathrm{AB,C}}), \tag{24}$$

where $[\theta_{\min}, \theta_{\max}]$ is the region where the sequential fragmentation events do not overlap with other channels. To determine the number of concerted fragmentation events, $N_{\mathrm{conc.}}$, we subtract the number of events in all sequential fragmentation channels, i.e., all possible intermediate molecules, from the total number of three-body breakup events.

As previously mentioned, the assumption that $N(\theta_{\mathrm{AB,C}})$ is uniform for all $\theta_{\mathrm{AB,C}}$ is not exactly fulfilled in our experiment since dips exist around $\theta_{\mathrm{AB,C}} = 0°$ and 180° for both sequential processes. Furthermore, in Appendix A we provide a simple model describing one possible origin for the dips. This model also shows that the $N(\theta_{\mathrm{AB,C}})$ distribution as well as the 'dips' are symmetric about 90°. Therefore, to accurately determine the number of sequential events, we need to take the dips into account. To do so, we select the region $[\theta_{\mathrm{low}}, \theta_{\mathrm{high}}]$ shown in Fig. 11(a) [100], which only includes the dips, and the region $[\theta_{\min}, \theta_{\max}]$ that selects the remaining separated sequential fragmentation events outside of the dips. Then, taking advantage of the reflection symmetry of $N(\theta_{\mathrm{AB,C}})$ about 90°, the total corrected number of sequential events are

$$N'_{\mathrm{AB,C}} = \frac{180 - 2\,(\theta_{\mathrm{high}} - \theta_{\mathrm{low}})}{\theta_{\max} - \theta_{\min}} \sum_{\theta_{\min}}^{\theta_{\max}} N(\theta_{\mathrm{AB,C}}) + 2 \sum_{\theta_{\mathrm{low}}}^{\theta_{\mathrm{high}}} N(\theta_{\mathrm{AB,C}}). \tag{25}$$

Then, $N_{\mathrm{conc.}}$ is determined by subtracting $N'_{\mathrm{AB,C}}$ for all sequential breakup channels from the total number of three-body fragmentation events.

We report the evaluated branching ratios in Table I. These measured branching ratios differ from the physical ones due to the limitations of the experiment, as is usually the case. Our experiment, for instance, is sensitive only to particular time windows for each step. Therefore, any comparison with theoretical results requires consideration of these limitations. In addition, we note that the two- and three-body breakup channels are corrected for their different detection efficiency, specifically (ε^2) and (ε^3), respectively. The single ion detection efficiency is

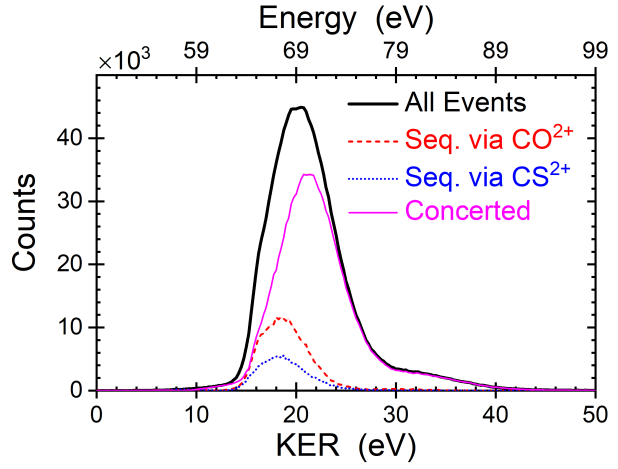

FIG. 10. (Color online) The separated N(KER) distributions for sequential and concerted fragmentation. The top axis represents the energy of the transient OCS^{3+} relative to the $X\,^1\Sigma^+(\boldsymbol{v}$=0,0,0) ground state of the neutral OCS molecule.

estimated to be $\varepsilon = 0.37 \pm 0.03$ by comparing the measured $O^+ + C^+ + S^+$ to the $C^+ + S^+$ ion pairs measured in coincidence, i.e., events where the O^+ fragment was "lost", as further explained in Ref. [101]. The reported errors in Table I include the statistical errors and the uncertainty in the detection efficiency.

Following triple ionization, the OCS molecule undergoes concerted three-body fragmentation into $O^+ + C^+ + S^+$ or sequential breakup, which is initiated by breaking into either $CO^{2+} + S^+$ or $CS^{2+} + O^+$ in the first breakup step. In the second step, the sequential fragmentation channels can either break into $O^+ + C^+ + S^+$ or the dication remains intact all the way to the detector. Sequential fragmentation involving the SO^{2+} molecule is not observed in our measurement (see further discussion in Sec. VI D).

V. SEQUENTIAL FRAGMENTATION RETRIEVAL ALGORITHM

The main advantage of analyzing three-body breakup using native frames and identifying sequential breakup as a uniform angular $N(\theta_{\mathrm{AB,C}})$ distribution is our ability to reconstruct the concealed sequential events by exploiting the uniform distribution. Below, we present an algorithm that reconstructs the whole sequential fragmentation distribution event-by-event, which allows one to separate competing sequential and concerted breakup in any plot created from the measured momenta. It is important to note that the reconstruction algorithm assumes that the rotation of the intermediate fragment occurs entirely in the fragmentation plane, which is not necessarily expected to be the case as explained in Sec. III.

Returning to the general ABC notation, our algorithm begins with selecting the clearly separated sequential events. Explicitly, we select the events within the range $\theta_{\mathrm{AB,C}} = [\theta_{\min}, \theta_{\max}]$ and $\mathrm{KER_{AB}} = [\mathrm{KER_{min}}, \mathrm{KER_{max}}]$. For example, the specific region used to select sequential fragmentation involving the CO^{2+} intermediate is $\theta_{\mathrm{CO,S}} = [8°, 45°]$ and $\mathrm{KER_{CO}} = [4, 11.5]$ eV, shown as the red rectangle in Fig. 11(a). The reconstruction of sequential fragmentation involving the CS^{2+} intermediate (using a selection procedure like for CO^{2+} above [102]) yields a similar figure (not shown for brevity).

The goal of the algorithm is to generate equivalent events from the measured events and reproduce the sequential fragmentation distributions in regions overlapping other competing processes. To accomplish this goal, one has to determine how many equivalent events should be created based on the number of measured events clearly identified as sequential breakup. Then, the equivalent events generated need to be assigned an angle $\theta_{\mathrm{AB,C}}$ randomly to produce a uniform angular distribution. These two key components are detailed below.

First, to determine how many equivalent sequential events must be generated from each measured event within $[\theta_{\min}, \theta_{\max}]$, we define the factor

$$F = \frac{180 - (\theta_{\max} - \theta_{\min})}{\theta_{\max} - \theta_{\min}}. \tag{26}$$

For sequential fragmentation involving CO^{2+}, $F = 3.86$, meaning each event within $\theta_{\mathrm{CO,S}} = [8°, 45°]$ creates, on average, 3.86 equivalent events outside this range. In practice, this is accomplished by generating either 3 or 4 equivalent events for each measured event, where the random choice between 3 or 4 is weighted by 16% to 86%, respectively, to yield the 3.86 average.

Second, to build a uniform distribution, we transform each equivalent event to the body-fixed xyz coordinate system given by Eqs. (14)–(16), where $\theta_{\mathrm{AB,C}}$ is defined in the xy plane as shown in Fig. 12. Since $N(\theta_{\mathrm{AB,C}})$ is uniform, we rotate each event to a new, randomly selected, $\theta'_{\mathrm{AB,C}}$, given by

$$\theta'_{\mathrm{AB,C}} \equiv r(180 + \theta_{\min} - \theta_{\max}) + \theta_{\max} \pmod{180}, \tag{27}$$

outside the $[\theta_{\min}, \theta_{\max}]$ region, shown in Fig. 12(b). In Eq. 27, r is a random number uniformly distributed between $[0, 1]$. This rotation is performed while maintaining $|\boldsymbol{p}_{\mathrm{AB}}|$ constant and preserving the conjugate momentum associated with the first step, i.e., $\boldsymbol{p}_{\mathrm{AB,C}}$. If done correctly, the distributions inside and outside the $[\theta_{\min}, \theta_{\max}]$ region should have the same average density of counts. The equivalent events maintain the statistical fluctuations of the original data set since they are generated using the data and are rotated randomly.

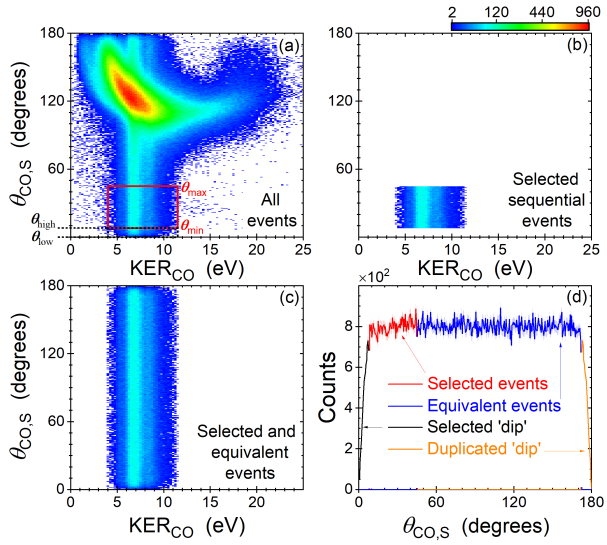

FIG. 11. (Color online) The $N(\mathrm{KER_{CO}}, \theta_{\mathrm{CO,S}})$ distributions for (a) all $O^+ + C^+ + S^+$ events, (b) the selected sequential events used to generate equivalent events, (c) the full sequential fragmentation distribution including the selected and reconstructed equivalent events, and (d) the $N(\theta_{\mathrm{CO,S}})$ distributions for the different steps of the reconstruction algorithm integrated over $\mathrm{KER_{CO}}$.

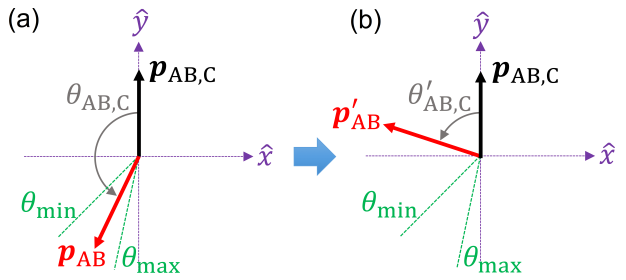

FIG. 12. (Color online) A schematic for reconstructing equivalent events. (a) an original measured sequential event is depicted (see text). (b) an equivalent event, which is just the original event rotated to a new, randomly generated, $\theta'_{\mathrm{AB,C}}$ angle. Note that $\boldsymbol{p}_{\mathrm{AB}}$ only spans the space for $x \leq 0$ due to the definition of the fragmentation plane.

The new conjugate momentum describing the second fragmentation step is given by

$$\boldsymbol{p}'_{\mathrm{AB}} = |\boldsymbol{p}_{\mathrm{AB}}| \left(-\sin\theta'_{\mathrm{AB,C}}\,\hat{\boldsymbol{x}} + \cos\theta'_{\mathrm{AB,C}}\,\hat{\boldsymbol{y}}\right). \tag{28}$$

To determine the momenta of each individual fragment in the CM frame of the ABC molecule, we first transform the momenta from the body-fixed frame (i.e., xyz coordinates) to the lab-fixed frame (i.e., XYZ coordinates). Then, we solve Eqs. (6, 8, 10) for $\boldsymbol{P}_{\mathrm{A}}$, $\boldsymbol{P}_{\mathrm{B}}$, and $\boldsymbol{P}_{\mathrm{C}}$. With these momenta, we can determine the sequential fragmentation via AB + C contributions in any plot.

The algorithm described above generates a uniform $N(\theta_{\mathrm{AB,C}})$ distribution over all $\theta_{\mathrm{AB,C}}$. However, our data contains dips located at $\theta_{\mathrm{CO,S}} = 0$ and 180°, as seen in Fig. 3(a-b). We explain the origin of these dips in Appendix A using a simple model, which also indicates that the dips are symmetric about $\theta_{\mathrm{AB,C}} = 90°$. To account for the dips, we modify our algorithm using a similar approach as detailed in Sec. IV D. Specifically, we select the data contained in the dip on the edge where the sequential fragmentation events are clearly identified, given by the gate $[\theta_{\mathrm{low}}, \theta_{\mathrm{high}}] = [0, 8°]$ for the CO^{2+} intermediate. Then we duplicate and rotate the events to $\theta'_{\mathrm{CO,S}} = 180 - \theta_{\mathrm{CO,S}}$ to preserve the shape of the dip. Because of its "copy and paste" nature, this reconstruction of the dip is statistically inferior to the sequential event reconstruction describe above, and it may even introduce artifacts. As the dip is a small fraction of the distribution, however, the quality degradation is minimal. The reconstructed $N(\mathrm{KER_{CO}}, \theta_{\mathrm{CO,S}})$ distribution is shown in Fig. 11(c), while the resulting $N(\theta_{\mathrm{CO,S}})$ distributions for each step of the reconstruction algorithm are detailed in Fig. 11(d).

The crux of this algorithm is that we retrieve the sequential fragmentation distribution in regions obscured by other competing fragmentation mechanisms by exploiting the uniform $N(\theta_{\mathrm{AB,C}})$ distribution. Since the algorithm works event-by-event and provides the momentum of each fragment, any plot can be created showing the contributions of each sequential fragmentation mechanism separately. It is important to note that the reconstruction algorithm only properly reproduces the distribution for states that have long enough lifetimes to create a uniform angular distribution.

In Sec. VI, we take the reconstruction algorithm presented above a step further and subtract the sequential fragmentation contributions from several plots containing all events, revealing the detailed behavior of concerted and sequential breakup beyond their identification and branching ratios discussed in Sec. IV. To judge how well the reconstruction method works, we examine the quality of the subtractions to ensure no over-subtraction of the sequential breakup distributions occur, as shown in Appendix C.

VI. SEPARATING CONCERTED AND SEQUENTIAL EVENTS: COMPARISON OF METHODS

In this section, we demonstrate the strength of applying the native-frames approach, where its extension allows us to separate concerted from sequential fragmentation in any plot created from the measured momenta. In particular, we show how to properly subtract the sequential breakup contributions in the $N(\mathrm{KER_{AB}}, \theta_{\mathrm{AB,C}})$ plots, revealing the structures associated with concerted fragmentation. Additionally, we show that the reconstruction algorithm accurately reproduces the expected sequential fragmentation distributions in both Newton diagrams and Dalitz plots, and that sequential fragmentation via the $SO^{2+} + C^{+}$ is negligible under the conditions of our experiment.

A. Native-frames analysis

In Fig. 13(a–d), we plot the $N(\mathrm{KER_{CO}}, \theta_{\mathrm{CO,S}})$ distribution and show the contributions of concerted breakup as well as sequential fragmentation involving the CO^{2+} and CS^{2+} intermediates. To determine the contributions of concerted fragmentation, shown in Fig. 13(b), the sequential breakup distributions in Fig. 13(c) and Fig. 13(d) are subtracted from the plot containing all events shown in Fig. 13(a). The analysis quantifying the quality of the resulting concerted breakup plot is discussed in Appendix C. The subtraction reveals that the large feature centered at $\theta_{\mathrm{CO,S}} = 120°$ is mostly due to concerted breakup. There is also a feature in Fig. 13(a) extending over a wide $\mathrm{KER_{CO}}$ range, overlapping (partly) the concerted-breakup peak, which arises from analyzing the sequential fragmentation via $CS^{2+} + O^{+}$ in the incorrect frame [this feature is shown separately in Fig. 13(d)].

Note that the remaining density plots of the separated channels shown in this paper always follow the style of Fig. 13(a-d). Explicitly, the top left panel represents the entire data set, the top right panel contains the concerted breakup contributions while the bottom left and right

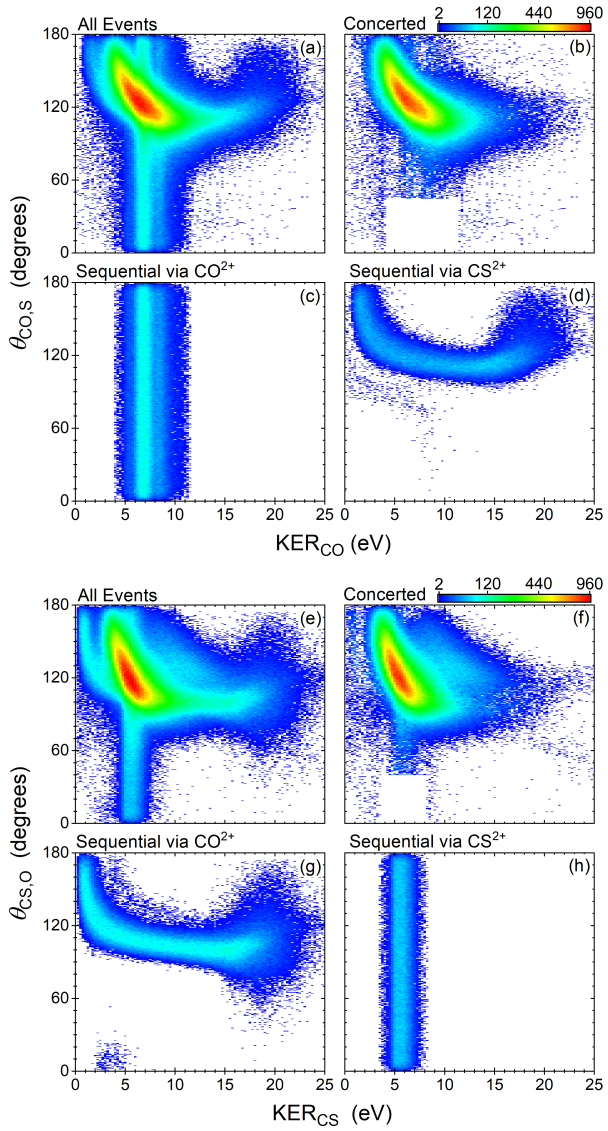

FIG. 13. (Color online) (a–d) The $N(\mathrm{KER}_{\mathrm{CO}}, \theta_{\mathrm{CO,S}})$ distributions for (a) all $O^+ + C^+ + S^+$ events, (b) concerted fragmentation, and sequential fragmentation via (c) $CO^{2+} + S^+$ and (d) $CS^{2+} + O^+$. Note that panel (b) shows the difference between panel (a) and the bottom two panels, which in turn show reconstructed data (see text). (e-h) The same as panels (a–d), but plotted for CS^{2+} intermediate, specifically for (e) all events, (f) concerted fragmentation events, and sequential fragmentation via (g) $CO^{2+} + S^+$ and (h) $CS^{2+} + O^+$. Note the sharp "cuts" in panels (b) and (d) that indicate imperfections in the subtraction procedure as detailed in the text and Appendix C. These features are at the few-counts (below 1%) level.

show the sequential fragmentation distributions via the $CO^{2+} + S^+$ and $CS^{2+} + O^+$ channels, respectively. Remnants of the sequential breakup are still visible in the concerted breakup distributions in Figs. 13(b) and 13(f). These remnants are generally at the level of the subtraction error, however. The same holds for other figures implementing the same subtraction procedure below.

Similarly, we plot in Fig. 13(e-h) the separated contributions of the concerted and sequential fragmentation distributions in the CS native frame. Here, too, the concerted breakup contributions appear as a feature centered at $\theta_{\mathrm{CS,O}} = 120°$ while the curved distribution originating at low $\mathrm{KER}_{\mathrm{CS}}$ comes from the sequential fragmentation involving the CO^{2+} intermediate.

Next, we utilize the sequential and concerted fragmentation channels, separated using native frames analysis as shown in Fig. 13, and plot them using the more traditional schemes, namely Newton diagrams and Dalitz plots, to illustrate how each of these channels appears in these presentations.

B. Newton diagrams

In a Newton diagram the sequential breakup is identified as a circular feature due to the rotation of the intermediate in the fragmentation plane [50]. To analyze sequential fragmentation via the CO^{2+} intermediate, we choose to fix the momentum of the S^+ fragment along the x axis, while the C^+ and O^+ momenta are divided by $|\boldsymbol{P}_{\mathrm{S}}|$ and placed in the upper and lower halves of the plot, respectively, as shown in Fig. 14(a). Figure 14(c) displays the expected offset semi-circle for sequential fragmentation via $CO^{2+} + S^+$. The "sprinkler" shape extending to large relative momenta is due to sequential fragmentation involving the CS^{2+} molecule, as shown separately in Fig. 14(d). The concerted fragmentation contributions, shown in Fig. 14(b), demonstrate that the breakup is not co-linear, suggesting some bending of the linear OCS molecule. Moreover, the O^+ fragment has nearly the same momentum (∼85%) as the S^+ fragment, and they are breaking almost back-to-back, while the C^+ fragment, experiencing forces in opposite directions, gains less momentum, as one would expect from a simple Coulomb explosion modeling of a slightly bent OCS.

Likewise, to analyze sequential fragmentation via the CS^{2+} intermediate, the O^+ momentum is chosen to be along the x axis of the Newton diagram while the C^+ and S^+ are scaled by $|\boldsymbol{P}_{\mathrm{O}}|$ and placed in the upper and lower halves, respectively, as shown in Fig. 14(e). The CS^{2+} sequential channel also appears as an offset semi-circle, shown in Fig. 14(h). The other sequential channel involving the CO^{2+} intermediate emerges as a sprinkler-like feature in Fig. 14(g). The concerted fragmentation distribution, shown in Fig. 14(f), is similar to the results shown in Fig. 14(b).

C. Dalitz plots

As stated above, the Dalitz plot depicts energy sharing between the fragments [66]. In the case of OCS breaking

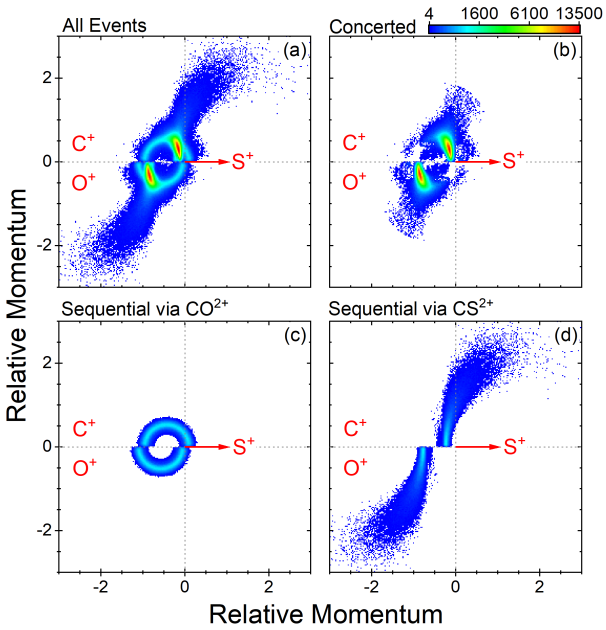

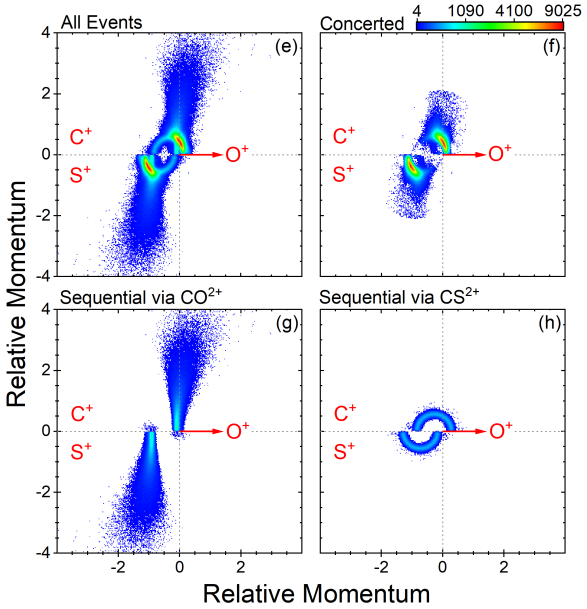

FIG. 14. (Color online) Newton diagrams with the S^+ momentum fixed along the x axis for (a) all $O^+ + C^+ + S^+$ events, (b) concerted fragmentation, and sequential fragmentation via (c) $CO^{2+} + S^+$ and (d) $CS^{2+} + O^+$. Similar Newton diagrams but with the O^+ momentum fixed along the x axis for (e) all $O^+ + C^+ + S^+$ events, (f) concerted fragmentation, and sequential fragmentation via (g) $CO^{2+} + S^+$ and (h) $CS^{2+} + O^+$.

into $O^+ + C^+ + S^+$, Wales *et al.* [55] identified the features in the Dalitz plot associated with sequential fragmentation involving the CO^{2+} and CS^{2+} intermediate molecules. In this brief section, we show that the results of our analysis are consistent with their results.

We show the Dalitz plots of the separated concerted

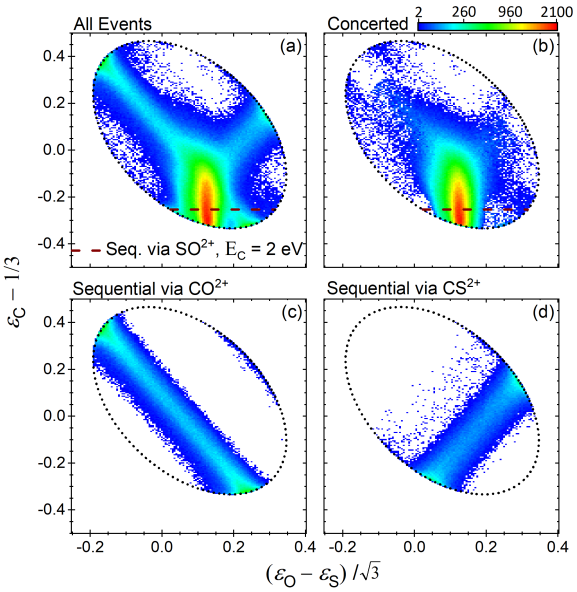

FIG. 15. (Color online) Dalitz plots for (a) all $O^+ + C^+ + S^+$ events, (b) concerted fragmentation, and sequential fragmentation via (c) $CO^{2+} + S^+$ and (d) $CS^{2+} + O^+$. The brown dashed line in panels (a-b) marks the expected location of sequential fragmentation via the SO^{2+} intermediate assuming $E_C = 2\,\text{eV}$ and a total KER of 20 eV (see Sec. VI D).

and sequential fragmentation distributions in Fig. 15, following the same choice of axes used by Wales *et al.* [55]. Recall that ε_i represents the scaled energy of fragment i relative to the center-of-mass of the molecule, that is the kinetic energy of that fragment divided by the total kinetic energy release in the OCS^{3+} fragmentation. In particular, we observe straight line distributions due to the sequential fragmentation channels involving the CO^{2+} and CS^{2+} intermediate molecules, as shown in Fig. 15(c) and Fig. 15(d), respectively. The concerted distribution in Fig. 15(b), which is a broad feature peaked at approximately $(0.125, -0.295)$ and extending to larger $\varepsilon_C - 1/3$ values, shows that the C^+ fragment accounts for a larger fraction of the total KER than the ∼0.3% expected for a linear geometry. This suggests that bending of the OCS molecule plays a role during concerted fragmentation.

This finding is consistent with the other visualization methods described above though the signatures differ. Recall that the indication for bending was that the momentum distributions peaked away from the expected linear breakup, for example $\theta_{CO,S}$ peaking away from 180° in native frames analysis — the simplicity of the signature in the momentum imaging methods is worth noting.

D. Is there sequential fragmentation via $SO^{2+} + C^+$?

One would expect a low rate, if any, for sequential fragmentation of OCS^{3+} via $SO^{2+} + C^+$ since it requires

bond formation between the two end atoms. This less likely bond-rearrangement process has been observed in double ionization of some triatomic molecules [101, 103, 104]. In this section, we use the native-frames method to verify that this sequential channel is negligible in our experiment, while illustrating the method for identifying sequential fragmentation.

First, we plot the $N(\mathrm{KER}_{\mathrm{SO}}, \theta_{\mathrm{SO,C}})$ distributions in Fig. 16(a), and observe a vertical stripe centered around $\mathrm{KER}_{\mathrm{SO}} = 18\,\mathrm{eV}$. Hereafter, we refer to this feature as the "stripe". The relatively narrow $\mathrm{KER}_{\mathrm{SO}}$ distribution of this stripe, supported by its nearly uniform angular distribution in $\theta_{\mathrm{SO,C}}$, suggest that sequential fragmentation via the SO^{2+} intermediate may be occurring. The $\mathrm{KER}_{\mathrm{SO}}$ values are much higher than the $\lesssim$10 eV expected for SO^{2+} [105], thus raising doubts if this sequential breakup truly occurs in our experiment.

To further test if sequential fragmentation via the SO^{2+} intermediate occurs, we plot the $N(\gamma_{\mathrm{SO}}, \theta_{\mathrm{SO,C}})$ distribution in Fig. 17(a). Recall that γ_{SO} is the Euler angle between the N-axis and X-axis defined in Sec. III C [see Fig. 5(d)]. Figure 17(a) exhibits a clear dependence of the $N(\theta_{\mathrm{SO,C}})$ distribution on the angle γ_{SO}, indicating that the apparent sequential fragmentation via $SO^{2+} + C^+$ is not independent of the orientation of the fragmentation plane as it should. This suggests that sequential breakup via an intermediate SO^{2+} molecule is not observed in our experiment.

To determine the source of the stripe, visible in Fig. 16(a), we show the separated concerted- and sequential-fragmentation distributions in Fig. 16(b-d). These figures demonstrate that the stripe, centered about 18 eV, is accidental, as it is due to a combination of sequential breakup via CO^{2+} and CS^{2+}, shown in Fig. 16(c-d), respectively. Note that part of this accidental stripe is still visible in Fig. 16(b), which shows the concerted fragmentation after subtraction of the sequential-breakup channels shown in Fig. 16(c-d), however, this leftover feature is on the level of the subtraction error.

Another indicator that the observed stripe is not due to sequential fragmentation via SO^{2+} is provided by the channel separated $N(\gamma_{\mathrm{SO}}, \theta_{\mathrm{SO,C}})$ distributions shown in Fig. 17. It is evident from this figure that the stripe is not independent of γ_{SO} as it should for a SO^{2+} intermediate rotating in the fragmentation plane. The observed γ_{SO} dependence of the stripe occurs because $\boldsymbol{p}_{\mathrm{SO,C}}$ is not aligned along the projection of the polarization into the fragmentation plane, as is the case for the $\boldsymbol{p}_{\mathrm{CO,S}}$ and $\boldsymbol{p}_{\mathrm{CS,O}}$ conjugate momenta. Instead, it rotates in space since the $\boldsymbol{p}_{\mathrm{SO,C}}$ momentum is related to the other sequential processes that exhibit the observe tilt when plotted versus γ_{SO}, as shown in Fig. 17(c-d).

Finally, we call attention to the fact that some SO^{2+} states are predicted to have very long lifetimes [105] (though no lifetimes are computed explicitly in Ref. [105]). Moreover, this metastable dication has been observed recently in $SO_2^{2+} \rightarrow SO^{2+} + O$ photodissociation [106] experiments with comparable TOF as in our setup (i.e., a few microseconds). Therefore, we expect that if SO^{2+} is formed in the first fragmentation step of OCS^{3+}, some of the metastable SO^{2+} molecules should survive all the way to the detector, resulting in $SO^{2+} + C^+$ coincidence events. In our experiment, only 79 events passed the momentum conservation conditions for this channel, about the level of random-

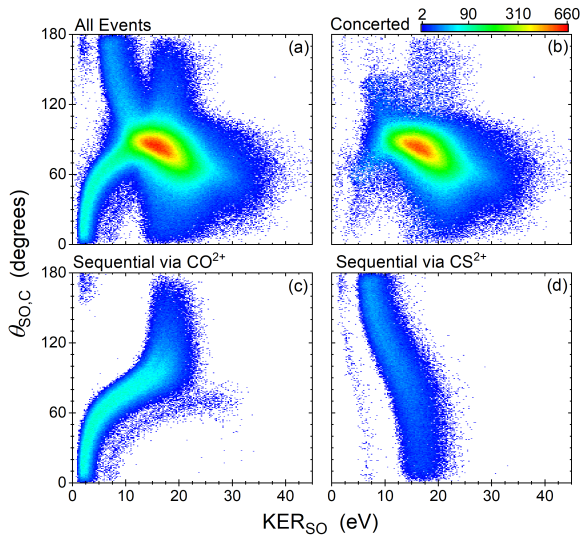

FIG. 16. (Color online) The $N(\mathrm{KER}_{\mathrm{SO}}, \theta_{\mathrm{SO,C}})$ distributions for (a) all $O^+ + C^+ + S^+$ events, (b) concerted fragmentation, and sequential fragmentation via (c) $CO^{2+} + S^+$ and (d) $CS^{2+} + O^+$. The magenta dashed lines at 18 eV indicate the apparent uniform $N(\theta_{\mathrm{SO,C}})$ distribution.

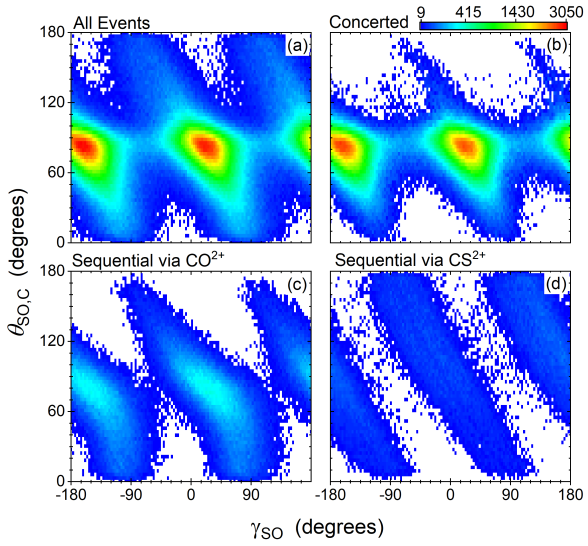

FIG. 17. (Color online) The $N(\gamma_{\mathrm{SO}}, \theta_{\mathrm{SO,C}})$ distributions for (a) all $O^+ + C^+ + S^+$ events, (b) concerted fragmentation, and sequential fragmentation via (c) $CO^{2+} + S^+$ and (d) $CS^{2+} + O^+$. Note that the $N(\gamma_{\mathrm{SO}}, \theta_{\mathrm{SO,C}})$ distributions for the sequential breakup via CO^{2+} and CS^{2+} are tilted (see text).

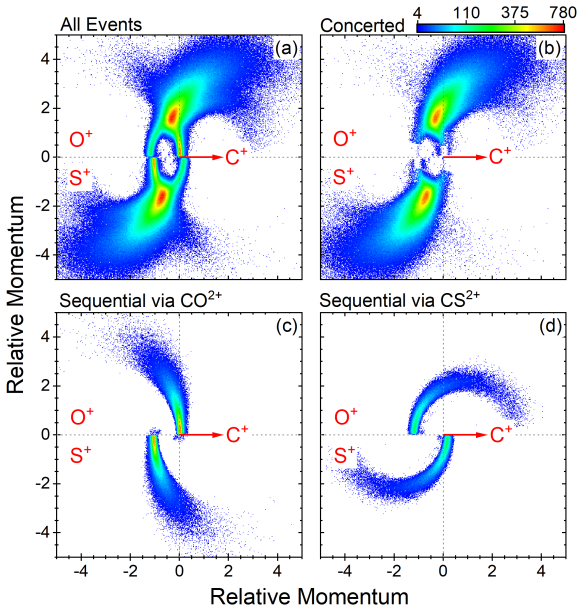

FIG. 18. (Color online) Newton diagrams with the C^+ fragment fixed to the x axis (see text) for (a) all $O^+ + C^+ + S^+$ events, (b) concerted fragmentation, and sequential fragmentation via (c) $CO^{2+} + S^+$ and (d) $CS^{2+} + O^+$.

coincidence events. Moreover, if these are true events then the $SO^{2+} + C^+$ channel is about 7×10^{-4} times smaller than each of the other sequential breakup channels, i.e., $CO^{2+} + S^+$ and $CS^{2+} + O^+$. Though we cannot exclude sequential breakup via SO^{2+} completely, we can safely state that it has an extremely low rate in our experiment.

For comparison, we investigate whether or not Newton diagrams or Dalitz plots can better determine if this unlikely process occurs. To use the Newton diagram for identifying sequential fragmentation via the SO^{2+} intermediate, the C^+ momentum is set along the x axis while the O^+ and S^+ momenta are divided by $|\boldsymbol{P}_C|$ and plotted in the upper and lower halves of the figure, respectively. The Newton diagram, shown in Fig. 18(a), exhibits a circular feature suggesting that sequential fragmentation via $SO^{2+} + C^+$ does occur. In reality, this feature is again accidental resulting from the other sequential fragmentation channels shown in Fig. 18(c-d), and vanishing upon their subtraction as demonstrated in Fig. 18(b).

Similarly, the Dalitz plot does not help identify if sequential fragmentation via $SO^{2+} + C^+$ occurs, but for a different reason. The distribution resulting from this sequential breakup should be centered around a constant ε_C because the energy of the C^+, ejected during the first fragmentation step, is independent of the rotation of the SO^{2+} intermediate. Using the peaks of the measured total KER and KER_{SO}, the center of the distribution associated with the SO^{2+} intermediate in the Dalitz plot is predicted to be located around $(\varepsilon_C - 1/3) = -0.233$, marked by the brown dotted line in Fig. 15(a). This location is simulated assuming that $E_C = 2$ eV due to energy conservation and using the information that the total KER is centered at approximately 20 eV, as we show in Fig. 10. Based on the Dalitz plot, we cannot exclude the sequential channel involving the SO^{2+} intermediate until the other sequential channels are subtracted, as shown in Fig. 15(b). However, if the C^+ fragment acquired a larger fraction of the total KER than was assumed above, the Dalitz plot may facilitate the unique identification of sequential breakup via the SO^{2+} intermediate.

Finally, we note that without the ability to subtract the CO^{2+} and CS^{2+} sequential breakup contributions, these conclusions about SO^{2+} sequential breakup would be difficult to reach. It is also worth mentioning that the accidental strip around $KER_{SO} \sim 18$ eV would not prevent the observation of sequential breakup via SO^{2+} as that is expected to form a stripe at lower KER_{SO} (<10 eV) [105], and that underscores the fact that we use both the angular distribution and expected KER to identify and separate sequential breakup.

VII. SUMMARY

This paper details the native-frames analysis method, which we apply to identify and separate sequential and concerted fragmentation, as proposed in our previous publication [37]. Explicitly, the native frames analysis method is based on the use of the conjugate momenta of the relevant Jacobi coordinates, i.e., the relative momenta. In addition, to identify the sequential breakup we use the KER in the second fragmentation step, and the rotation of the intermediate molecule in the fragmentation plane as the signature. This rotation results in a uniform $N(\theta_{AB,C})$ distribution. The advantage of our analysis is that it allows the separation of competing sequential and concerted fragmentation distributions, which may be vital for interpreting experiments. In addition, the method provides information about the sequential and concerted breakup mechanisms.

Since we introduced the native frames analysis method [37], it has been applied, for instance, in molecular fragmentation studies induced by photon [36, 81, 82, 107–112], electron [113, 114] and ion [115–119] impact. These examples demonstrate the broad applicability of the native-frames analysis in understanding molecular dynamics. The detailed description of this method, presented in this paper, should help researchers to take full advantage of this analysis method.

As the molecular imaging community moves toward measuring more complex molecules and higher-fold coincidence channels, researchers need to be mindful of possible contributions due to sequential fragmentation. In the case when polyatomic molecules are multiply ionized, the formation of metastable molecules with lifetimes of picoseconds or longer are likely to occur [120–122]. Therefore, sequential fragmentation can play a non-negligible role in three- or more-body fragmentation, ne-

cessitating the ability to identify and separate its contributions from concerted fragmentation. Furthermore, the native-frames methodology can be methodically generalized to four- and more-body fragmentation channels using Jacobi coordinates, thus providing scientists with additional methods for visualizing their data, regardless if the molecule fragments through sequential or concerted breakup processes.

ACKNOWLEDGMENTS

We thank C. W. Fehrenbach for assistance with the PULSAR laser. This work is supported by the Chemical Sciences, Geosciences, and Biosciences Division, Office of Basic Energy Sciences, Office of Science, U.S. Department of Energy under Award number DE-FG02-86ER13491, and the PULSAR laser was provided by Grant DE-FG02-09ER16115 from the same funding agency.

Appendix A: Modeling $N(\theta_{\mathrm{AB,C}})$ distribution

Throughout the paper, we assumed that the rotation of the AB intermediate molecule occurs in the fragmentation plane. As a result, even though $\theta_{\mathrm{AB,C}}$ represents a polar angle in spherical coordinates, the signature of sequential fragmentation is a nearly uniform $N(\theta_{\mathrm{AB,C}})$ distribution instead of a uniform $N(\cos\theta_{\mathrm{AB,C}})$ distribution, which is the signature of an isotropic distribution as discussed in Sec. III C. We illustrate in Fig. 19 that the momentum, $\boldsymbol{p}_{\mathrm{AB}}$, probability distribution is a ring produced by the rotation and breakup of the AB molecule in the fragmentation plane.

The thickness of the ring is mainly attributed to the resolution of the measured momenta. This assessment is based on the large difference between the width of these "edge dips" between sequential dissociation of D_2O^{2+} to $D^+ + D^+ + O$ and $D^+ + O^+ + D$, both occurring via an OD^+ intermediate molecule [82]. The momentum resolution of the latter channel is inferior and the dips are much larger. This assessment is supported by simulations presented in Appendix C of Ref. [82]. That said, we cannot exclude that in some cases other factors, such as high initial angular momentum, may also play a role, and further investigations are needed.

In this appendix, we explore the consequences of describing the ring distribution as a function of the spherical polar angle θ, which is equivalent to the angle $\theta_{\mathrm{AB,C}}$ between the two conjugate momenta. Specifically, we demonstrate that the thickness of this thin ring leads to dips at the edges of the $N(\theta_{\mathrm{AB,C}})$ distributions, similar to what we observe experimentally.

The ring distribution, shown in Fig. 19, is modeled using Gaussian distributions and is explicitly written as

$$\Phi(x,y,z) \propto \exp\left[-\frac{1}{2}\left(\frac{\rho-\rho_0}{\Delta}\right)^2\right]\exp\left[-\frac{1}{2}\left(\frac{y}{\Delta}\right)^2\right], \tag{A1}$$

where ρ_0 is the radius of the ring in the XZ plane, Δ is the width in each direction, and ρ is given by

$$\rho = \sqrt{x^2+z^2}. \tag{A2}$$

Note that we set the width of the ring to be the same in both directions, which simplifies the following math significantly. Converting the expression to spherical coordinates gives

$$\Phi(r,\theta,\phi) \propto \exp\left[-\frac{1}{2}\left(\frac{r\chi-\rho_0}{\Delta}\right)^2 - \frac{1}{2}\left(\frac{r^2(1-\chi^2)}{\Delta}\right)^2\right], \tag{A3}$$

with

$$\chi \equiv \frac{\rho}{r} = \sqrt{1-\sin^2\theta\,\sin^2\phi}\,, \tag{A4}$$

where θ and ϕ are the standard polar and azimuthal angles in spherical coordinates.

To determine the expected angular distribution $N(\theta)$, we integrate the function Φ over the radial and azimuthal coordinates assuming that $\rho_0 \gg \Delta$, i.e., the distribution width is small compared to its centroid. This approximation makes possible the analytic result

$$\Phi(\theta) \propto e^{-\beta\,\eta}\,\left[\,(2-\eta)\,I_0(\beta\,\eta) + \eta\,I_1(\beta\,\eta)\,\right], \tag{A5}$$

where $I_n(\beta\,\eta)$ are the modified Bessel functions while η and β are defined by

$$\eta = \sin^2\theta\,, \tag{A6}$$

$$\beta = \frac{\rho_0^2}{2\Delta^2}\,. \tag{A7}$$

We find that $\Phi(\theta)$ is symmetric about $\theta = \pi/2$ as one would expect.

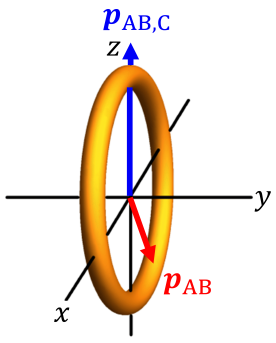

FIG. 19. (Color online) The isosurface of the $\boldsymbol{p}_{\mathrm{AB}}$ probability distribution given by Eq. A1. Specifically, the surface is for a constant value of $\Phi = 0.5$, where $\Delta = 0.5$ and $\rho_0 = 4$.

Then, to plot the distribution of $N(\theta)$, we multiply $\Phi(\theta)$ by the volume element $\sin\theta$, resulting in the distribution shown in Fig. 20 for a few values of ρ_0/Δ. Note that the distribution shown is normalized, i.e., $\int_0^\pi N(\theta)\,d\theta = 1$, and it is plotted as a function of $\theta_{\rm AB,C}$, which as stated above is the same as θ.

This model reproduces the dips at the edges of the distribution. Furthermore, we see small peaks next to the dips that we do not observe experimentally, most likely because of the reduced detection efficiency around the detector center, which affects mainly events with $\theta_{\rm AB,C}$ as we discussed in Sec. III C.

It is important to mention that we do not need to incorporate the volume element, $\sin\theta$, in our experimental data because it is naturally accounted for when binning the data.

Appendix B: Classical model — point charges–rigid rotor interaction

In this appendix, we describe the classical model used to determine the angular momentum gained by a heteronuclear diatomic molecule interacting with a point charge. Specifically, we use the sequential fragmentation of OCS via the CO^{2+} intermediate as an example. In this case, the angular momentum gain is perpendicular to the molecular plane due to the interaction between the permanent dipole of CO^{2+} and the S^+ fragment ejected in the first step, which is treated as a point charge.

In Fig. 21 we show a diagram of the initial conditions immediately after the rapid triple ionization of OCS, where we assume no stretching of the C–O and C–S bonds, i.e., equilibrium distances in the neutral OCS, given by $R_{\rm CO} = 2.19$ and $R_{\rm CS} = 2.95$ a.u., respectively [123]. On the other hand, the bond angle ξ_i, which is 180° for the equilibrium geometry of OCS, is used as a parameter. For the linear equilibrium configuration, the S^+ fragment does not apply any torque on the CO^{2+} fragment, hence the CO^{2+} molecule does not gain any angular momentum. In contrast, if the OCS molecule is bent, even slightly, the CO^{2+} does experience a torque and quickly gains significant angular momentum.

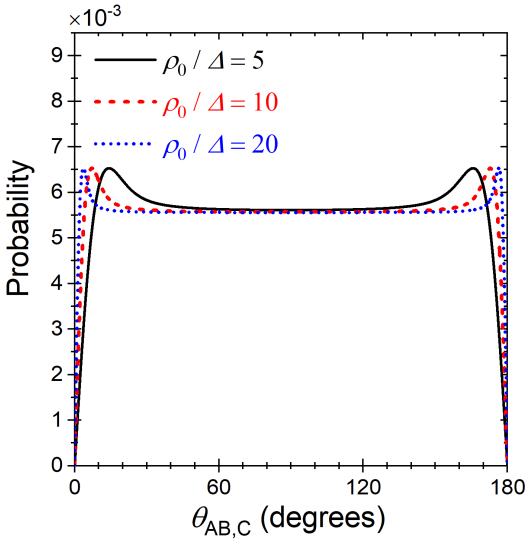

FIG. 20. (Color online) The normalized probability distribution $N(\theta) = \sin\theta\,\Phi(\theta)$ for $\rho_0/\Delta = 5, 10$, and 20.

In order to compute the angular momentum gained by the CO^{2+}, we model it as a rigid rotor having two point charges, $q_{\rm C}$ and $q_{\rm O}$, separated by $R_{\rm CO}$. To evaluate the charges $q_{\rm C}$ and $q_{\rm O}$, we use the calculated permanent dipole of the CO^{2+} ground electronic state at $R_{\rm CO} = 2.19$ a.u., which is $D \simeq 3$ Debye [124] (with similar values for other low-lying states). For the origin defined at the CM of the CO^{2+} molecule, we approximate the dipole as

$$D = R_{\rm CO}\left(\delta q + \frac{1}{7}\right), \tag{B1}$$

where $q_{\rm C} = 1 + \delta q \simeq 1.4$ and $q_{\rm O} = 1 - \delta q \simeq 0.6$ a.u. Furthermore, we neglect the motion of the fragments associated with the molecule's initial vibration and rotation, which are expected to be cold in the He seeded supersonic jet used in the experiment. Specifically, the translational temperature is estimated from the width of the center-of-mass momenta to be about 10-20 K [6, 82, 125]. The internal temperature, vibrational and rotational, is expected to be similar due to collisions in the jet. So, we expect the target OCS molecule population to be in its vibrational ground state with only a few low-lying rotational states.

Due to the mutual Coulomb repulsion and conservation of linear momentum, the S^+ and CO^{2+} undergo back-to-back breakup. The translational and rotational motion is described by a set of coupled differential equations that we propagate in time. Specifically, we use the "ode45" function in MATLAB, which is based on the Runge-Kutta method, to solve the equations of motion numerically. We assume that the motion starts from rest at $t = 0$ a.u. at the internuclear distances associated with the equilibrium of the neutral molecule and neglect any initial angular momentum. The propagation of the equations of motion is terminated after 3×10^4 a.u. (i.e., about 725 fs) when the distance between the two fragments exceeds 350 a.u., at which time the CO^{2+} velocity and an-

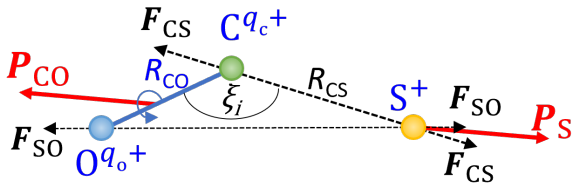

FIG. 21. (Color online) Schematic diagram of a bent OCS^{3+} leading to rotation of the CO^{2+} fragment (see text). The black-dashed arrows marks the Coulomb forces' direction.

gular momentum converge to a constant value (smaller than 0.1 % deviations).

The calculated angular momentum of the intermediate CO^{2+} as a function of initial bond angle ξ_i is shown in Fig. 22(a). It can be clearly seen that the final angular momentum increases rapidly with bending of the OCS, resulting in a few tens of $\hbar$ for bending angles smaller than 177°. Moreover, the time evolution shown in Fig. 22(b) indicates that this angular momentum is gained in a couple hundred femtoseconds.

At this point it is reasonable to wonder what is causing such bending in a vibrationally cold linear OCS molecule. It seems the natural explanation is that the laser pulse is exciting some bending of the molecule before all three electrons are stripped. The specific underlying excitation mechanism is not known, and it is still being investigated, but the evidence for bending is provided also by the fact that concerted fragmentation peaks far from the $\theta_{AB,C} = 180°$ expected for collinear breakup (see Fig. 13).

Appendix C: Quantifying the quality of the separated concerted breakup plots

In this Appendix, we discuss how to evaluate the quality of the subtractions leading to the separated concerted fragmentation plots. This analysis allows one to determine if the reconstruction algorithm accurately reproduces the sequential distributions by looking for over or under subtraction. As an example, we discuss the error in the concerted fragmentation $N(\mathrm{KER_{CO}}, \theta_{\mathrm{CO,S}})$ distribution. A similar analysis needs to be conducted for every concerted breakup plot to determine what features are statistically significant.

The separated concerted fragmentation plots are computed by subtracting the sequential fragmentation distributions from the distribution of all $O^+ + C^+ + S^+$ events. To quantify the error of the resulting concerted fragmentation distribution, statistical errors are propagated through the subtraction pixel-by-pixel to determine the error map.

In Fig. 23(a) and Fig. 23(b), the respective positive and negative values of the concerted fragmentation distributions are displayed. In particular, Fig. 23(b) shows that, in some regions, we over-subtract the sequential-breakup contributions. To determine if the over-subtraction is statistically significant, we divide, pixel-by-pixel, the yields N_{ij} by their error σ_{ij}, i.e., N_{ij}/σ_{ij}, as shown in Figs. 23(c) and Figs. 23(d) for positive and negative values, respectively. If $|N_{ij}/\sigma_{ij}| \leq 2$, the value of the pixel is consistent with zero, within the subtraction error at a 95.45% confidence level. Since the majority of pixels in Fig. 23(d) are less than 2σ from zero, we conclude that the negative values resulting from the subtraction are within the statistical fluctuations of our data set.

Even though only the statistical analysis for the $N(\mathrm{KER_{CO}}, \theta_{\mathrm{CO,S}})$ distribution is discussed in this Appendix, a similar analysis was conducted for every concerted breakup plot presented in this paper and in Ref. [37]. The quality of all the plots mentioned above are consistent with the example shown in this appendix.

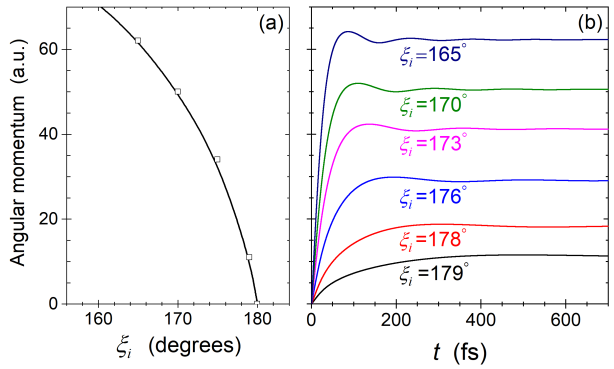

FIG. 22. (Color online) (a) Calculated final angular momentum of the CO^{2+} intermediate fragment of OCS as a function of the initial bond angle ξ_i. (b) The time evolution of the total angular momentum of the CO^{2+} for a few values of ξ_i. Note that angular momentum conservation holds for the whole $S^+ + CO^{2+}$ system.

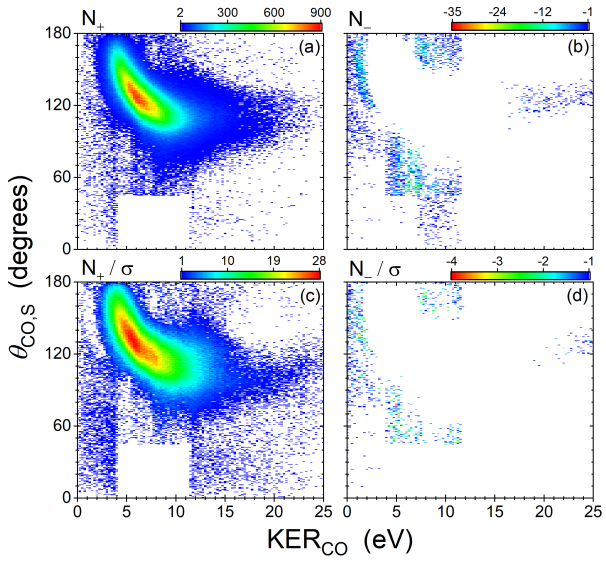

FIG. 23. (Color online) Characterization of the quality of the concerted fragmentation $N(\mathrm{KER_{CO}}, \theta_{\mathrm{CO,S}})$ distribution. Plots of the (a) positive and (b) negative values of the $N(\mathrm{KER_{CO}}, \theta_{\mathrm{CO,S}})$ distribution, and the similar (c) positive and (d) negative distributions determined by dividing the yields of each pixel N_{ij} by their error σ_{ij}.

[1] B. Whitaker, ed., *Imaging in Molecular Dynamics - Technology and Applications* (Cambridge University Press, New York, NY, 2003).

[2] J. Ullrich, ed., *Ten years of COLTRIMS and Reaction Microscopes* (Max-Planck-Institut fur Kernphysic Heidelbergy, Heidelberg, Germany, 2004).

[3] G. E. Hall and P. L. Houston, Vector correlations in photodissociation dynamics, Annual Review of Physical Chemistry **40**, 375 (1989), and references therein.

[4] Z. Vager, R. Naaman, and E. P. Kanter, Coulomb explosion imaging of small molecules, Science **244**, 426 (1989).

[5] A. J. R. Heck and D. W. Chandler, Imaging techniques for the study of chemical reaction dynamics, Annual Review of Physical Chemistry **46**, 335 (1995), and references therein.

[6] J. Ullrich, R. Moshammer, R. Dörner, O. Jagutzki, V. Mergel, H. Schmidt-Böcking, and L. Spielberger, Recoil-ion momentum spectroscopy, Journal of Physics B: Atomic, Molecular and Optical Physics **30**, 2917 (1997).

[7] R. E. Continetti, Coincidence spectroscopy, Annual Review of Physical Chemistry **52**, 165 (2001).

[8] J. Ullrich, R. Moshammer, A. Dorn, R. Dörner, L. P. H. Schmidt, and H. Schmidt-Böcking, Recoil-ion and electron momentum spectroscopy: Reaction-microscopes, Reports on Progress in Physics **66**, 1463 (2003).

[9] T. Weber, A. O. Czasch, O. Jagutzki, A. K. Müller, V. Mergel, A. Kheifets, E. Rotenberg, G. Meigs, M. H. Prior, S. Daveau, A. Landers, C. L. Cocke, T. Osipov, R. Díez Muiño, H. Schmidt-Böcking, and R. Dörner, Complete photo-fragmentation of the deuterium molecule, Nature **431**, 437 (2004).

[10] D. Townsend, S. A. Lahankar, S. K. Lee, S. D. Chambreau, A. G. Suits, X. Zhang, J. Rheinecker, L. B. Harding, and J. M. Bowman, The roaming atom: Straying from the reaction path in formaldehyde decomposition, Science **306**, 1158 (2004).

[11] I. Ben-Itzhak, P. Q. Wang, J. F. Xia, A. M. Sayler, M. A. Smith, K. D. Carnes, and B. D. Esry, Dissociation and ionization of H_2^+ by ultrashort intense laser pulses probed by coincidence 3D momentum imaging, Phys. Rev. Lett. **95**, 073002 (2005).

[12] D. Rolles, M. Braune, S. Cvejanović, O. Geßner, R. Hentges, S. Korica, B. Langer, T. Lischke, G. Prümper, A. Reinköster, J. Viefhaus, B. Zimmermann, V. McKoy, and U. Becker, Isotope-induced partial localization of core electrons in the homonuclear molecule N_2, Nature **437**, 711 (2005).

[13] M. F. Kling, C. Siedschlag, A. J. Verhoef, J. I. Khan, M. Schultze, T. Uphues, Y. Ni, M. Uiberacker, M. Drescher, F. Krausz, and M. J. J. Vrakking, Control of electron localization in molecular dissociation, Science **312**, 246 (2006).

[14] F. Martín, J. Fernández, T. Havermeier, L. Foucar, T. Weber, K. Kreidi, M. Schöffler, L. Schmidt, T. Jahnke, O. Jagutzki, A. Czasch, E. P. Benis, T. Osipov, A. L. Landers, A. Belkacem, M. H. Prior, H. Schmidt-Böcking, C. L. Cocke, and R. Dörner, Single photon-induced symmetry breaking of H_2 dissociation, Science **315**, 629 (2007).

[15] D. Akoury, K. Kreidi, T. Jahnke, T. Weber, A. Staudte, M. Schöffler, N. Neumann, J. Titze, L. P. H. Schmidt, A. Czasch, O. Jagutzki, R. A. C. Fraga, R. E. Grisenti, R. D. Muiño, N. A. Cherepkov, S. K. Semenov, P. Ranitovic, C. L. Cocke, T. Osipov, H. Adaniya, J. C. Thompson, M. H. Prior, A. Belkacem, A. L. Landers, H. Schmidt-Böcking, and R. Dörner, The simplest double slit: Interference and entanglement in double photoionization of H_2, Science **318**, 949 (2007).

[16] E. Garand, J. Zhou, D. E. Manolopoulos, M. H. Alexander, and D. M. Neumark, Nonadiabatic interactions in the Cl + H_2 reaction probed by ClH_2^- and ClD_2^- photoelectron imaging, Science **319**, 72 (2008).

[17] M. S. Schöffler, J. Titze, N. Petridis, T. Jahnke, K. Cole, L. P. H. Schmidt, A. Czasch, D. Akoury, O. Jagutzki, J. B. Williams, N. A. Cherepkov, S. K. Semenov, C. W. McCurdy, T. N. Rescigno, C. L. Cocke, T. Osipov, S. Lee, M. H. Prior, A. Belkacem, A. L. Landers, H. Schmidt-Böcking, T. Weber, and R. Dörner, Ultrafast probing of core hole localization in N_2, Science **320**, 920 (2008).

[18] J. D. Savee, V. A. Mozhayskiy, J. E. Mann, A. I. Krylov, and R. E. Continetti, The role of excited-state topology in three-body dissociation of sym-triazine, Science **321**, 826 (2008).

[19] A. S. Sandhu, E. Gagnon, R. Santra, V. Sharma, W. Li, P. Ho, P. Ranitovic, C. L. Cocke, M. M. Murnane, and H. C. Kapteyn, Observing the creation of electronic Feshbach resonances in soft x-ray–induced O_2 dissociation, Science **322**, 1081 (2008).

[20] J. McKenna, A. M. Sayler, B. Gaire, N. G. Johnson, K. D. Carnes, B. D. Esry, and I. Ben-Itzhak, Benchmark measurements of H_3^+ nonlinear dynamics in intense ultrashort laser pulses, Phys. Rev. Lett. **103**, 103004 (2009).

[21] G. Sansone, F. Kelkensberg, J. F. Pérez-Torres, F. Morales, M. F. Kling, W. Siu, O. Ghafur, P. Johnsson, M. Swoboda, E. Benedetti, F. Ferrari, F. Lépine, J. L. Sanz-Vicario, S. Zherebtsov, I. Znakovskaya, A. L'Huillier, M. Y. Ivanov, M. Nisoli, F. Martin, and M. J. J. Vrakking, Electron localization following attosecond molecular photoionization, Nature **465**, 763 (2010).

[22] M. P. Grubb, M. L. Warter, H. Xiao, S. Maeda, K. Morokuma, and S. W. North, No straight path: Roaming in both ground- and excited-state photolytic channels of $NO_3 \rightarrow NO + O_2$, Science **335**, 1075 (2012).

[23] M. Pitzer, M. Kunitski, A. S. Johnson, T. Jahnke, H. Sann, F. Sturm, L. P. H. Schmidt, H. Schmidt-Böcking, R. Dörner, J. Stohner, J. Kiedrowski, M. Reggelin, S. Marquardt, A. Schießer, R. Berger, and M. S. Schöffler, Direct determination of absolute molecular stereochemistry in gas phase by Coulomb explosion imaging, Science **341**, 1096 (2013).

[24] J. A. DeVine, M. L. Weichman, B. Laws, J. Chang, M. C. Babin, G. Balerdi, C. Xie, C. L. Malbon, W. C. Lineberger, D. R. Yarkony, R. W. Field, S. T. Gibson, J. Ma, H. Guo, and D. M. Neumark, Encoding of vinylidene isomerization in its anion photoelectron spectrum, Science **358**, 336 (2017).

[25] C. E. M. Strauss and P. L. Houston, Correlations with-

out coincidence measurements: Deciding between stepwise and concerted dissociation mechanisms for ABC → A + B + C, The Journal of Physical Chemistry **94**, 8751 (1990), and references therein.
[26] C. Maul and K.-H. Gericke, Photo induced three body decay, International Reviews in Physical Chemistry **16**, 1 (1997), and references therein.
[27] R. N. Zare, Dissociation of H_2^+ by electron impact: Calculated angular distribution, The Journal of Chemical Physics **47**, 204 (1967).
[28] R. R. Lucchese, A. Lafosse, J. C. Brenot, P. M. Guyon, J. C. Houver, M. Lebech, G. Raseev, and D. Dowek, Polar and azimuthal dependence of the molecular frame photoelectron angular distributions of spatially oriented linear molecules, Phys. Rev. A **65**, 020702 (2002).
[29] D. Dowek, M. Lebech, J. Houver, and R. Lucchese, Photoemission in the molecular frame using the vector correlation approach: From valence to inner-valence shell ionization, Journal of Electron Spectroscopy and Related Phenomena **141**, 211 (2004), frontiers of Coincidence Experiments.
[30] D. Toffoli, R. R. Lucchese, M. Lebech, J. C. Houver, and D. Dowek, Molecular frame and recoil frame photoelectron angular distributions from dissociative photoionization of NO_2, The Journal of Chemical Physics **126**, 054307 (2007), and references therein.
[31] R. Guillemin, P. Decleva, M. Stener, C. Bomme, T. Marin, L. Journel, T. Marchenko, R. K. Kushawaha, K. Jänkälä, N. Trcera, K. P. Bowen, D. W. Lindle, M. N. Piancastelli, and M. Simon, Selecting core-hole localization or delocalization in CS_2 by photofragmentation dynamics, Nature Communications **6**, 6166 (2015).
[32] R. N. Zare, Photoejection dynamics, Molecular Photochemistry **4**, 1 (1972).
[33] T. P. Rakitzis and R. N. Zare, Photofragment angular momentum distributions in the molecular frame: Determination and interpretation, The Journal of Chemical Physics **110**, 3341 (1999).
[34] A. Hishikawa, H. Hasegawa, and K. Yamanouchi, Sequential three-body Coulomb explosion of CS_2 in intense laser fields appearing in momentum correlation map, Chemical Physics Letters **361**, 245 (2002).
[35] N. Ferreira, L. Sigaud, and E. C. Montenegro, Three-body fragmentation from single ionization of water by electron impact: The role of satellite states, The Journal of Physical Chemistry A **121**, 3234 (2017).
[36] S. Pathak, R. Obaid, S. Bhattacharyya, J. Bürger, X. Li, J. Tross, T. Severt, B. Davis, R. C. Bilodeau, C. A. Trallero-Herrero, A. Rudenko, N. Berrah, and D. Rolles, Differentiating and quantifying gas-phase conformational isomers using Coulomb explosion imaging, The Journal of Physical Chemistry Letters **11**, 10205 (2020).
[37] J. Rajput, T. Severt, B. Berry, B. Jochim, P. Feizollah, B. Kaderiya, M. Zohrabi, U. Ablikim, F. Ziaee, Kanaka Raju P., D. Rolles, A. Rudenko, K. D. Carnes, B. D. Esry, and I. Ben-Itzhak, Native frames: Disentangling sequential from concerted three-body fragmentation, Phys. Rev. Lett. **120**, 103001 (2018).
[38] A. M. Sayler, E. Eckner, J. McKenna, B. D. Esry, K. D. Carnes, I. Ben-Itzhak, and G. G. Paulus, Nonunique and nonuniform mapping in few-body coulomb-explosion imaging, Phys. Rev. A **97**, 033412 (2018).
[39] Z. L. Streeter, F. L. Yip, R. R. Lucchese, B. Gervais, T. N. Rescigno, and C. W. McCurdy, Dissociation dynamics of the water dication following one-photon double ionization. I. theory, Physical Review A **98**, 053429 (2018).
[40] D. Reedy, J. B. Williams, B. Gaire, A. Gatton, M. Weller, A. Menssen, T. Bauer, K. Henrichs, P. Burzynski, B. Berry, Z. L. Streeter, J. Sartor, I. Ben-Itzhak, T. Jahnke, R. Dörner, T. Weber, and A. L. Landers, Dissociation dynamics of the water dication following one-photon double ionization. II. experiment, Physical Review A **98**, 053430 (2018).
[41] F. Anis, T. Cackowski, and B. D. Esry, Rotational dynamics of dissociating H_2^+ in a short intense laser pulse, Journal of Physics B: Atomic, Molecular and Optical Physics **42**, 091001 (2009).
[42] P. M. Kroger and S. J. Riley, Dynamics of three body half collisions. I. secondary product decomposition in the photodissociation of acetyl iodide, The Journal of Chemical Physics **67**, 4483 (1977).
[43] U. Werner, K. Beckord, J. Becker, and H. O. Lutz, 3D imaging of the collision-induced Coulomb fragmentation of water molecules, Phys. Rev. Lett. **74**, 1962 (1995).
[44] S. Hsieh and J. H. D. Eland, Reaction dynamics of three-body dissociations in triatomic molecules from single-photon double ionization studied by a time- and position-sensitive coincidence method, Journal of Physics B: Atomic, Molecular and Optical Physics **30**, 4515 (1997).
[45] A. Hishikawa, H. Hasegawa, and K. Yamanouchi, Nuclear dynamics on the light-dressed potential energy surface of CS_2 by coincidence momentum imaging, Chemical Physics Letters **388**, 1 (2004).
[46] A. Hishikawa, M. Ueyama, and K. Yamanouchi, Probing the ultrafast nuclear motion in CS_2^{2+} in intense laser fields, The Journal of Chemical Physics **122**, 151104 (2005).
[47] M. Ueyama, H. Hasegawa, A. Hishikawa, and K. Yamanouchi, Concerted and sequential Coulomb explosion processes of N_2O in intense laser fields by coincidence momentum imaging, The Journal of Chemical Physics **123**, 154305 (2005).
[48] P. Liu, T. Okino, Y. Furukawa, T. Ichikawa, R. Itakura, K. Hoshina, K. Yamanouchi, and H. Nakano, Three-body sequential Coulomb explosions of CH_3OD^{3+} induced by intense laser fields, Chemical Physics Letters **423**, 187 (2006).
[49] A. Matsuda, M. Fushitani, R. D. Thomas, V. Zhaunerchyk, and A. Hishikawa, Multiple explosion pathways of the deuterated benzene trication in 9-fs intense laser fields, The Journal of Physical Chemistry A **113**, 2254 (2009).
[50] N. Neumann, D. Hant, L. P. H. Schmidt, J. Titze, T. Jahnke, A. Czasch, M. S. Schöffler, K. Kreidi, O. Jagutzki, H. Schmidt-Böcking, and R. Dörner, Fragmentation dynamics of CO_2^{3+} investigated by multiple electron capture in collisions with slow highly charged ions, Phys. Rev. Lett. **104**, 103201 (2010).
[51] J. Wu, M. Kunitski, L. P. H. Schmidt, T. Jahnke, and R. Dörner, Structures of N_2Ar, O_2Ar, and O_2Xe dimers studied by Coulomb explosion imaging, The Journal of Chemical Physics **137**, 104308 (2012).
[52] L. Zhang, S. Roither, X. Xie, D. Kartashov, M. Schöffler, H. Xu, A. Iwasaki, S. Gräfe, T. Okino, K. Yamanouchi, A. Baltuska, and M. Kitzler, Path-

selective investigation of intense laser-pulse-induced fragmentation dynamics in triply charged 1,3-butadiene, Journal of Physics B: Atomic, Molecular and Optical Physics **45**, 085603 (2012).
[53] C. Wu, C. Wu, D. Song, H. Su, Y. Yang, Z. Wu, X. Liu, H. Liu, M. Li, Y. Deng, Y. Liu, L.-Y. Peng, H. Jiang, and Q. Gong, Nonsequential and sequential fragmentation of CO_2^{3+} in intense laser fields, Phys. Rev. Lett. **110**, 103601 (2013).
[54] R. Karimi, E. Bisson, B. Wales, S. Beaulieu, M. Giguére, Z. Long, W.-K. Liu, J.-C. Kieffer, F. Légaré, and J. Sanderson, N_2O ionization and dissociation dynamics in intense femtosecond laser radiation, probed by systematic pulse length variation from 7 to 500 fs, The Journal of Chemical Physics **138**, 204311 (2013).
[55] B. Wales, E. Bisson, R. Karimi, S. Beaulieu, A. Ramadhan, M. Giguére, Z. Long, W.-K. Liu, J.-C. Kieffer, F. Légaré, and J. Sanderson, Coulomb imaging of the concerted and stepwise break up processes of OCS ions in intense femtosecond laser radiation, Journal of Electron Spectroscopy and Related Phenomena **195**, 332 (2014).
[56] A. Matsuda, E. J. Takahashi, and A. Hishikawa, Time-resolved laser Coulomb explosion imaging using few-cycle intense laser pulses: Application to exploding CS_2 in highly charged states, Journal of Electron Spectroscopy and Related Phenomena **195**, 327 (2014).
[57] A. Khan, L. C. Tribedi, and D. Misra, Observation of a sequential process in charge-asymmetric dissociation of CO_2^{q+} $(q = 4, 5)$ upon the impact of highly charged ions, Phys. Rev. A **92**, 030701 (2015).
[58] E. Wang, X. Shan, Z. Shen, M. Gong, Y. Tang, Y. Pan, K.-C. Lau, and X. Chen, Pathways for nonsequential and sequential fragmentation of CO_2^{3+} investigated by electron collision, Phys. Rev. A **91**, 052711 (2015).
[59] S. Yan, X. L. Zhu, P. Zhang, X. Ma, W. T. Feng, Y. Gao, S. Xu, Q. S. Zhao, S. F. Zhang, D. L. Guo, D. M. Zhao, R. T. Zhang, Z. K. Huang, H. B. Wang, and X. J. Zhang, Observation of two sequential pathways of CO_2^{3+} dissociation by heavy-ion impact, Phys. Rev. A **94**, 032708 (2016).
[60] A. Khan and D. Misra, Decay dynamics of N_2O under the impact of fast electrons, Journal of Physics B: Atomic, Molecular and Optical Physics **49**, 055201 (2016).
[61] A. Ramadhan, B. Wales, R. Karimi, I. Gauthier, M. MacDonald, L. Zuin, and J. Sanderson, Ultrafast molecular dynamics of dissociative ionization in OCS probed by soft x-ray synchrotron radiation, Journal of Physics B: Atomic, Molecular and Optical Physics **49**, 215602 (2016).
[62] Z. Shen, E. Wang, M. Gong, X. Shan, and X. Chen, Fragmentation dynamics of carbonyl sulfide in collision with 500 ev electron, The Journal of Chemical Physics **145**, 234303 (2016).
[63] U. Ablikim, C. Bomme, E. Savelyev, H. Xiong, R. Kushawaha, R. Boll, K. Amini, T. Osipov, D. Kilcoyne, A. Rudenko, N. Berrah, and D. Rolles, Isomer-dependent fragmentation dynamics of inner-shell photoionized difluoroiodobenzene, Phys. Chem. Chem. Phys. **19**, 13419 (2017).
[64] A. Khan, L. C. Tribedi, and D. Misra, Three-body fragmentation of multiply charged nitrous oxide induced by Ar^{8+}- and Xe^{15+}-ion impact, Phys. Rev. A **96**, 012703 (2017).
[65] X. Ding, M. Haertelt, S. Schlauderer, M. S. Schuurman, A. Y. Naumov, D. M. Villeneuve, A. R. W. McKellar, P. B. Corkum, and A. Staudte, Ultrafast dissociation of metastable CO^{2+} in a dimer, Phys. Rev. Lett. **118**, 153001 (2017).
[66] R. Dalitz, CXII. on the analysis of τ-meson data and the nature of the τ-meson, The London, Edinburgh, and Dublin Philosophical Magazine and Journal of Science **44**, 1068 (1953).
[67] A. Abele *et al.*, The ρ-mass, width and line shape in $\bar{p}p$ annihilation at rest into $\pi^+\pi^-\pi^0$ decays, Physics Letters B **469**, 270 (1999).
[68] R. Aaij *et al.*, Measurements of CP violation in the three-body phase space of charmless $B^{\pm}$ decays, Physical Review D **90**, 112004 (2014).
[69] B. Antolković and Z. Dolenec, The neutron-induced $^{12}C(n, n\prime)3\alpha$ reaction at 14.4 MeV in a kinematically complete experiment, Nuclear Physics A **237**, 235 (1975).
[70] R. Álvarez-Rodríguez, A. S. Jensen, E. Garrido, D. V. Fedorov, and H. O. U. Fynbo, Momentum distributions of α particles from decaying low-lying ^{12}C resonances, Physical Review C **77**, 064305 (2008).
[71] K. Ogata, M. Kan, and M. Kamimura, Quantum three-body calculation of the nonresonant triple-α reaction rate at low temperatures, Progress of Theoretical Physics **122**, 1055 (2009).
[72] O. S. Kirsebom, M. Alcorta, M. J. G. Borge, M. Cubero, C. A. Diget, R. Dominguez-Reyes, L. M. Fraile, B. R. Fulton, H. O. U. Fynbo, S. Hyldegaard, B. Jonson, M. Madurga, A. M. Martin, T. Nilsson, G. Nyman, A. Perea, K. Riisager, and O. Tengblad, Breakup of ^{12}C resonances into three α particles, Physical Review C **81**, 064313 (2010).
[73] J. Refsgaard, H. Fynbo, O. Kirsebom, and K. Riisager, Three-body effects in the Hoyle-state decay, Physics Letters B **779**, 414 (2018).
[74] R. Álvarez-Rodríguez, A. S. Jensen, E. Garrido, and D. V. Fedorov, Structure and three-body decay of ^9Be resonances, Physical Review C **82**, 034001 (2010).
[75] C. Lin, Hyperspherical coordinate approach to atomic and other Coulombic three-body systems, Physics Reports **257**, 1 (1995).
[76] J. Z. H. Zhang, *Theory and Application of Quantum Molecular Dynamics* (WORLD SCIENTIFIC, 1998).
[77] P. Cornille, *Advanced Electromagnetism and Vacuum Physics* (WORLD SCIENTIFIC, 2003).
[78] D. J. Tannor, *Introduction to Quantum Mechanics: A Time-Dependent Perspective* (University Science Books, 2007).
[79] Y. Wang, Ph.D. thesis, Kansas State University (2010).
[80] NIST Chemistry WebBook, SRD 69, [online]. Available: https://webbook.nist.gov/cgi/inchi?ID=C463581&Mask=20.
[81] T. Severt, Z. L. Streeter, W. Iskandar, K. A. Larsen, A. Gatton, D. Trabert, B. Jochim, B. Griffin, E. G. Champenois, M. M. Brister, D. Reedy, D. Call, R. Strom, A. L. Landers, R. Dörner, J. B. Williams, D. S. Slaughter, R. R. Lucchese, T. Weber, C. W. McCurdy, and I. Ben-Itzhak, Step-by-step state-selective tracking of fragmentation dynamics of water dications by momentum imaging, Nat. Commun. **13**, 5146 (2022).

[82] W. Iskandar, T. N. Rescigno, A. E. Orel, T. Severt, K. A. Larsen, Z. L. Streeter, B. Jochim, B. Griffin, D. Call, V. Davis, C. W. McCurdy, R. R. Lucchese, J. B. Williams, I. Ben-Itzhak, D. S. Slaughter, and T. Weber, Efficiency of charge transfer in changing the dissociation dynamics of OD^+ transients formed after the photo-fragmentation of D_2O, The Journal of Chemical Physics **159**, 094301 (2023).

[83] V. L. B. de Jesus, B. Feuerstein, K. Zrost, D. Fischer, A. Rudenko, F. Afaneh, C. D. Schröter, R. Moshammer, and J. Ullrich, Atomic structure dependence of nonsequential double ionization of He, Ne and Ar in strong laser pulses, Journal of Physics B: Atomic, Molecular and Optical Physics **37**, L161 (2004).

[84] Note that the A, B, and C labels represent atomic or molecular fragments, which may be neutral or charged.

[85] Note that a uniform $N(\cos\theta_{\mathrm{CO,S}})$ distribution is proportional to $\sin\theta_{\mathrm{CO,S}}$ when plotted in terms of $\theta_{\mathrm{CO,S}}$.

[86] The uniform $N(\theta_{\mathrm{CO,S}})$ distribution is proportional to $1/\sqrt{1-\cos^2\theta_{\mathrm{CO,S}}}$ when plotted in terms of $\cos\theta_{\mathrm{CO,S}}$.

[87] J. P. Bouhnik, I. Gertner, B. Rosner, Z. Amitay, O. Heber, D. Zajfman, E. Y. Sidky, and I. Ben-Itzhak, Measurements of the mean lifetime and kinetic-energy release of metastable CO^{2+}, Phys. Rev. A **63**, 032509 (2001), and private communication.

[88] M. Lundqvist, P. Baltzer, D. Edvardsson, L. Karlsson, and B. Wannberg, Novel time of flight instrument for Doppler free kinetic energy release spectroscopy, Phys. Rev. Lett. **75**, 1058 (1995).

[89] M. Hochlaf, R. Hall, F. Penent, H. Kjeldsen, P. Lablanquie, M. Lavollée, and J. Eland, Threshold photoelectrons coincidence spectroscopy of N_2^{2+} and CO^{2+} ions, Chemical Physics **207**, 159 (1996).

[90] T. Šedivcová, V. Špirko, and J. Fišer, Theoretical study of the CS^{2+} dication, J. Chem. Phys. **125**, 164308 (2006).

[91] T. Šedivcová, P. R. Žd'ánská, V. Špirko, and J. Fišer, Computed lifetimes of metastable states of CO^{2+}, The Journal of Chemical Physics **124**, 214303 (2006).

[92] J. H. D. Eland, M. Hochlaf, P. Linusson, E. Andersson, L. Hedin, and R. Feifel, Triple ionization spectra by coincidence measurements of double Auger decay: The case of OCS, The Journal of Chemical Physics **132**, 014311 (2010).

[93] A. Kramida, Yu. Ralchenko, J. Reader, and NIST ASD Team, NIST Atomic Spectra Database (ver. 5.6.1), [Online]. Available: `https://physics.nist.gov/asd` [2019, February 4]. National Institute of Standards and Technology, Gaithersburg, MD. (2018).

[94] B. Darwent, *Bond dissociation energies in simple molecules*, NSRDS-NBS31 No. iv, 48 p. (U.S. National Bureau of Standards; for sale by the Supt. of Docs., U.S. Govt. Print. Off., [Washington], 1970) pp. iv, 48 p.

[95] K. P. Huber and G. Herzberg, *Molecular Spectra and Molecular Structure— IV. Constants of Diatomic Molecules* (Van Nostrand Reinhold, 1979).

[96] G. Dawber, A. G. McConkey, L. Avaldi, M. A. MacDonald, G. C. King, and R. I. Hall, Threshold photoelectrons coincidence spectroscopy of doubly-charged ions of nitrogen, carbon monoxide, nitric oxide and oxygen, Journal of Physics B: Atomic, Molecular and Optical Physics **27**, 2191 (1994).

[97] E. Sidky and I. Ben-Itzhak, Phase-amplitude method for calculating resonance energies and widths for one-dimensional potentials, Phys. Rev. A **60**, 3586 (1999).

[98] L.-Y. C. Chiu, Electron magnetic perturbation in diatomic molecules of Hund's case b, The Journal of Chemical Physics **40**, 2276 (1964).

[99] C. G. Stevens and J. C. D. Brand, Angular momentum dependence of first and second order singlet triplet interactions in polyatomic molecules, The Journal of Chemical Physics **58**, 3324 (1973).

[100] For sequential fragmentation involving the CO^{2+} intermediate, the gated regions are $[\theta_{\min},\theta_{\max}] = [8°, 45°]$ and $[\theta_{\mathrm{low}},\theta_{\mathrm{high}}] = [0°, 8°]$.

[101] S. Zhao, B. Jochim, P. Feizollah, J. Rajput, F. Ziaee, Kanaka Raju P., B. Kaderiya, K. Borne, Y. Malakar, B. Berry, J. Harrington, D. Rolles, A. Rudenko, K. D. Carnes, E. Wells, I. Ben-Itzhak, and T. Severt, Strong-field induced bond rearragnement in triatomic molecules, Phys. Rev. A **99**, 053412 (2019).

[102] For sequential fragmentation involving the CS^{2+} intermediate, the gated regions are $[\theta_{\min},\theta_{\max}] = [7°, 40°]$ and $[\theta_{\mathrm{low}},\theta_{\mathrm{high}}] = [0°, 7°]$.

[103] J. Laksman, D. Céolin, M. Gisselbrecht, and S. L. Sorensen, Nuclear motion in carbonyl sulfide induced by resonant core electron excitation, The Journal of Chemical Physics **133**, 144314 (2010).

[104] S. Larimian, S. Erattupuzha, S. Mai, P. Marquetand, L. González, A. Baltuška, M. Kitzler, and X. Xie, Molecular oxygen observed by direct photoproduction from carbon dioxide, Physical Review A **95** (2017).

[105] A. Ben Houria, Z. Ben Lakhdar, M. Hochlaf, F. Kemp, and I. R. McNab, Theoretical investigation of the SO^{2+} dication and the photo-double ionization spectrum of SO, The Journal of Chemical Physics **122**, 054303 (2005).

[106] M. Jarraya, M. Wallner, G. Nyman, S. B. Yaghlane, M. Hochlaf, J. H. D. Eland, and R. Feifel, State selective fragmentation of doubly ionized sulphur dioxide, Scientific Reports **11**, 17137 (2021).

[107] X. Yu, X. Zhao, Z. Wang, Y. Yang, X. Zhang, P. Ma, X. Li, C. Wang, X. Xu, C. Wang, D. Zhang, S. Luo, and D. Ding, Determining the stereo configuration of carbonyl sulfide dimers using Coulomb-explosion imaging, Phys. Rev. A **104**, 053104 (2021).

[108] S. Bhattacharyya, K. Borne, F. Ziaee, S. Pathak, E. Wang, A. S. Venkatachalam, N. Marshall, K. D. Carnes, C. W. Fehrenbach, T. Severt, I. Ben-Itzhak, A. Rudenko, and D. Rolles, Two- and three-body fragmentation of multiply charged tribromomethane by ultrafast laser pulses, Phys. Chem. Chem. Phys. **24**, 27631 (2022).

[109] J. W. McManus, T. Walmsley, K. Nagaya, J. R. Harries, Y. Kumagai, H. Iwayama, M. N. Ashfold, M. Britton, P. H. Bucksbaum, B. Downes-Ward, T. Driver, D. Heathcote, P. Hockett, A. J. Howard, E. Kukk, J. W. L. Lee, Y. Liu, D. Milesevic, R. S. Minns, A. Niozu, J. Niskanen, A. J. Orr-Ewing, S. Owada, D. Rolles, P. A. Robertson, A. Rudenko, K. Ueda, J. Unwin, C. Vallance, M. Burt, M. Brouard, R. Forbes, and F. Allum, Disentangling sequential and concerted fragmentations of molecular polycations with covariant native frame analysis, Phys. Chem. Chem. Phys. **24**, 22699 (2022).

[110] R. Guillemin, T. Marin, M. Zmerli, C. Bomme, I. Ismail, L. Journel, T. Marchenko, O. Travnikova, M. N.

Piancastelli, and M. Simon, Concerted and sequential three-body fragmentation of deep-core-ionized carbon disulfide, Phys. Chem. Chem. Phys. **25**, 183 (2023).

[111] C. Cheng, L. J. Frasinski, G. m. c. Moǧol, F. Allum, A. J. Howard, D. Rolles, P. H. Bucksbaum, M. Brouard, R. Forbes, and T. Weinacht, Multiparticle cumulant mapping for Coulomb explosion imaging, Phys. Rev. Lett. **130**, 093001 (2023).

[112] V. Singh, C. Cheng, T. Weinacht, and S. Matsika, Quantum contributions to Coulomb-explosion imaging revealed by trajectory-surface-hopping molecular dynamics, Phys. Rev. A **109**, 052813 (2024).

[113] L. Chen, E. Wang, X. Shan, Z. Shen, X. Zhao, and X. Chen, Fragmentation of $CF_4{}^{q+}$ ($q = 2, 3$) induced by 1-keV electron collisions, Phys. Rev. A **104**, 032814 (2021).

[114] L. Chen, E. Wang, W. Zhao, M. Gong, X. Shan, and X. Chen, Fragmentation of SO_2^{q+} (q = 2–4) induced by 1 keV electron collision, The Journal of Chemical Physics **158**, 054301 (2023).

[115] C. Ma, S. Xu, D. Zhao, D. Guo, S. Yan, W. Feng, X. Zhu, and X. Ma, Three-body fragmentation dynamics of $CH_2CCH_2^{3+}$ investigated by 50-keV/u Ne^{8+} impact, Phys. Rev. A **101**, 052701 (2020).

[116] B. Wang, J. Han, X. Zhu, L. Wei, B. Ren, Y. Zhang, W. Yu, S. Yan, X. Ma, Y. Zou, L. Chen, and B. Wei, Dissociative ionization of OCS induced by highly charged ion impact, Phys. Rev. A **103**, 042810 (2021).

[117] H. Yuan, Z. Xu, S. Xu, C. Ma, Z. Zhang, D. Guo, X. Zhu, D. Zhao, S. Zhang, S. Yan, Y. Gao, R. Zhang, and X. Ma, Three-body fragmentation dynamics of CH_3CCH^{3+} investigated by 50-keV/u Ne^{8+} impact: Comparison with its isomer ion $CH_2CCH_2{}^{3+}$, Phys. Rev. A **105**, 022814 (2022).

[118] J. Yadav, C. P. Safvan, P. Bhatt, P. Kumari, A. Kumar, and J. Rajput, Hydrogen migration in triply charged acetylene, The Journal of Chemical Physics **156**, 141101 (2022).

[119] J. Yadav, C. P. Safvan, P. Bhatt, P. Kumari, J. Singh, and J. Rajput, Exploring three-body fragmentation of acetylene trication, The Journal of Chemical Physics **158**, 074302 (2023).

[120] S. D. Price, Interactions of molecular doubly charged ions with atoms, molecules and photons, J. Chem. Soc., Faraday Trans. **93**, 2451 (1997).

[121] D. Schröder and H. Schwarz, Generation, stability, and reactivity of small, multiply charged ions in the gas phase, The Journal of Physical Chemistry A **103**, 7385 (1999).

[122] S. D. Price, Investigating the gas-phase chemical reactions of molecular dications, Phys. Chem. Chem. Phys. **5**, 1717 (2003).

[123] G. Herzberg, *Electronic spectra and electronic structure of polyatomic molecules* (Van Nostrand, 1966).

[124] T. Šedivcová Uhlíková, P. R. Kaprálová-Žďánská, and V. Špirko, Radiative transition probabilities of CO^{2+}, International Journal of Quantum Chemistry **107**, 2654 (2007).

[125] A. Rudenko, V. Makhija, A. Vajdi, T. Ergler, M. Schürholz, R. K. Kushawaha, J. Ullrich, R. Moshammer, and V. Kumarappan, Strong-field-induced wave packet dynamics in carbon dioxide molecule, Faraday Discuss. **194**, 463 (2016).